

2015-04-29

CubeSat Design and Attitude Control with Micro Pulsed Plasma Thrusters

Ye Lu

Worcester Polytechnic Institute

Follow this and additional works at: <https://digitalcommons.wpi.edu/etd-theses>

Repository Citation

Lu, Ye, "CubeSat Design and Attitude Control with Micro Pulsed Plasma Thrusters" (2015). *Masters Theses (All Theses, All Years)*. 511.
<https://digitalcommons.wpi.edu/etd-theses/511>

This thesis is brought to you for free and open access by Digital WPI. It has been accepted for inclusion in Masters Theses (All Theses, All Years) by an authorized administrator of Digital WPI. For more information, please contact wpi-etd@wpi.edu.

CubeSat Design and Attitude Control with Micro Pulsed Plasma Thrusters

By

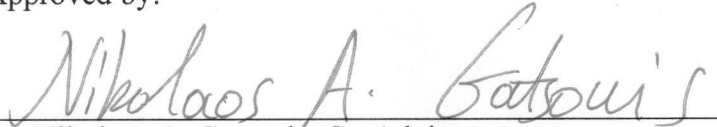
Ye Lu

A Thesis

Submitted to the Faculty of the
WORCESTER POLYTECHNIC INSTITUTE
in partial fulfilment of the requirements for the
Degree of Master of Science
in
Aerospace Engineering

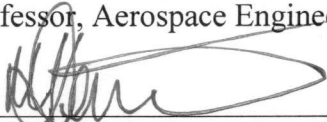

April 2015

Approved by:



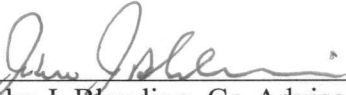
Dr. Nikolaos A. Gatsonis, Co-Advisor

Professor, Aerospace Engineering Program, Mechanical Engineering Department, WPI




Dr. Michael A. Demetriou, Co-Advisor

Professor, Aerospace Engineering Program, Mechanical Engineering Department, WPI



Dr. John J. Blandino, Co-Advisor

Associate Professor, Aerospace Engineering Program, Mechanical Engineering Department,
WPI



Dr. Seong-kyun Im, Graduate Committee Representative

Assistant Professor, Aerospace Engineering Program, Mechanical Engineering Department, WPI

Acknowledgement

I would like to express my very great appreciation to my thesis advisors, Professor Gatsonis for his guidance on the CubeSat and topnotch knowledge of μ PPT, and Professor Demetriou for his invaluable knowledge in control and estimation, without whom, this thesis would not have been possible. I also would like to thank Prof. Blandino for his important suggestions on the improvements in this work.

Through interaction with my advisors, I learned not only knowledge in engineering and science, but also how dedicated I should strive: every tiny detail is worth exploring and refining. This thesis work is a precious lesson and experience that I'll hold on for the rest of my career.

Abstract

This study presents the overall design of a 3U CubeSat equipped with commercial-off-the-shelf hardware, Teflon-fueled micro-Pulsed Plasma Thrusters (μ PPT) and an attitude determination and control system. The μ PPT is sized by the impulse bit and pulse frequency required for continuous compensation of expected maximum disturbance torques at altitudes between 400 and 1000 km, and to perform stabilization of up to 20 deg/s and slew maneuvers of up to 180 degrees. The study involves realistic power constraints anticipated on the 3U CubeSat. Attitude estimation is implemented using the q-method for static attitude determination of the quaternion using pairs of the spacecraft-sun and magnetic field vectors. The quaternion estimate and the gyroscope measurements are used with an extended Kalman filter to obtain the attitude estimates. Proportional and derivative control algorithms use the static attitude estimation in order to calculate the angular momentum required to compensate for the disturbance torques and to achieve specified stabilization and slewing maneuvers or combinations. Two control methods are developed: paired firing method, and separate control algorithm and thruster allocation methods which determines the optimal utilization of the available thrusters and introduces redundancy. Simulations results are presented for a 3U CubeSat under stabilization, pointing, and pointing and spinning scenarios.

Table of Contents

List of Figures.....	vii
List of Tables	x
Chapter 1. Introduction.....	1
1.1. Literature Review.....	2
1.2. Objectives and Approach.....	7
Chapter 2. CubeSat Design and Thruster Requirements	9
2.1. CubeSat Configuration.....	9
2.2. Reference Frames.....	10
2.3. Thruster Requirements for Disturbance Torques Compensation, Stabilization and Slew Maneuvers.....	13
2.3.1. Angular Momentum Evaluation	13
2.3.2. Impulse Bit and Pulse Frequency Requirements	18
2.4. μ PPT Design.....	22
Chapter 3. Attitude Dynamics, Estimation and Control	24
3.1. Attitude Dynamics and Estimation	25
3.2. Static Attitude Determination	26
3.2.1. Davenport's q-method	26
3.2.2. Sensors and Reference Models	28
3.3. Attitude Estimation with Extended Kalman Filtering (EKF).....	33
3.4. Attitude Control	36
3.4.1. Thruster Model and Control Implementation	36
3.4.2. Paired Firing Technique.....	39
3.4.3. Control using Separate Controller Algorithm and Thruster allocation.....	47
Chapter 4. Simulations of Mission Scenarios and Results	53
4.1. Input Parameters	53
4.2. Stabilization Results.....	54
4.3. Pointing Results	60
4.4. Pointing and Spinning Result.....	64

4.5. Pointing Performance with Thruster Failure.....	66
Chapter 5. Summary and Recommendations.....	71
5.1. Summary.....	71
5.2. Recommendations for Future Work.....	72
References.....	74

List of Figures

Figure 1-1: A 3U CubeSat with the μ PPT module located in the bottom 1U.	2
Figure 2-1: The 3U CubeSat with sun sensors are placed on +Y, -Y, -X and -Z faces.	10
Figure 2-2: Reference frames used in model, control and analysis.	12
Figure 2-3: Disturbance torques on a 3U CubeSat at altitudes from 300 to 1000 km.	16
Figure 2-4: Illustration for slew maneuver with definition of idle period.	17
Figure 2-5: Diagram representing idealized, thrust vs. time profile for a PPT pulse train.....	19
Figure 2-6: Angular momentum rate \dot{H} for different maneuvers of a given duration.	21
Figure 2-7: Requirement of impulse bit and pulse frequency at different angular momentum rate	22
Figure 2-8: Bottom 1U of CubeSat showing the thrusters comprising the μ PPT module.....	23
Figure 3-1: Flow chart for simulation, attitude determination and estimation.	26
Figure 3-2: Outline for extended Kalman filter algorithm.....	34
Figure 3-3: Top view of thruster arrangement (1, 2, 3, 4 are on the top layer).	37
Figure 3-4: Control strategy for stabilization using paired firing method	40
Figure 3-5: Control strategy for pointing using paired firing method	41
Figure 3-6: Depiction of optimal angular velocity threshold.....	43
Figure 3-7: Four policies featuring different angular velocity threshold vs error angle.....	43
Figure 3-8: Comparison of pointing accuracy with different policies.	44
Figure 3-9: Comparison of angular velocity profile for different policies for pointing.	45
Figure 3-10: Flow chart for attitude control.	48
Figure 4-1: Rotational kinetic energy of a CubeSat undergoing stabilization with paired firing (left) and thruster allocation (right).	55
Figure 4-2: Angular velocity of a 3U CubeSat undergoing stabilization with paired firing (left) and thruster allocation (right).	55
Figure 4-3: Firing sequence of μ PPTs on a 3U CubeSat during stabilization and compensation of periodic disturbance using paired firing; (Left) the total number of firings from	

each thruster; (Right) the time of occurrence for each firing indicted by a line. The areas filled with lines indicate that the specific thruster is on full operation. 56

- Figure 4-4: Firing sequence of μ PPTs on a 3U CubeSat during stabilization and compensation of periodic disturbance using thruster allocation; (Left) the total number of firings from each thruster; (Right) the time of occurrence for each firing indicted by a line. 57
- Figure 4-5: Power consumption of μ PPTs on a 3U CubeSat during stabilization and compensation of periodic disturbance torques with paired firing (left) and thruster allocation (right). 58
- Figure 4-6: Firing sequence of μ PPTs on a 3U CubeSat during stabilization and compensation of the maximum constant disturbance. (Left) The total number of firings from each thruster; (Right) the time of occurrence for each firing indicted by a line. 59
- Figure 4-7: Pointing angle error of a 3U CubeSat using μ PPTs with paired firing (left) and thruster allocation (right). 60
- Figure 4-8: Angular velocity of a 3U CubeSat undergoing pointing using μ PPTs with paired firing (left) and thruster allocation (right). 61
- Figure 4-9: Firing sequence of μ PPTs on a 3U CubeSat during pointing with paired firing allocation. (Left) The total number of firings from each thruster; (Right) the time of occurrence for each firing indicted by a line. 62
- Figure 4-10: Firing sequence of μ PPTs on a 3U CubeSat during pointing with thruster allocation. (Left) The total number of firings from each thruster; (Right) the time of occurrence for each firing indicted by a line. 63
- Figure 4-11: Power consumption of μ PPTs on a 3U CubeSat during pointing with paired firing (left) and thruster allocation (right). 63
- Figure 4-12: Pointing angle error of a 3U CubeSat undergoing spinning and pointing maneuvers using μ PPTs with paired firing (left) and thruster allocation (right). 64
- Figure 4-13: Angular velocity of a 3U CubeSat undergoing pointing and spinning to 3 deg/s using μ PPTs with paired firing (left) and thruster allocation (right). 65
- Figure 4-14: Power consumption of μ PPTs on a 3U CubeSat during pointing with paired firing (left) and thruster allocation (right). 65
- Figure 4-15: Angular velocity of a 3U CubeSat undergoing spinning to 3 deg/s without pointing using μ PPTs with thruster allocation. 66
- Figure 4-16: Pointing angle error of a 3U CubeSat using μ PPTs with paired firing (left) and thruster allocation (right) under thruster failure. 67
- Figure 4-17: Angular velocity of a 3U CubeSat using μ PPTs with paired firing (left) and thruster allocation (right) under thruster failure. 67

Figure 4-18: Power consumption of μ PPTs with paired firing (left) and thruster allocation (right) under thruster failure. 68

Figure 4-19: Pointing angle error of a 3U CubeSat using μ PPTs with paired firing (left) and thruster allocation (right) under two thruster failure. 68

Figure 4-20: Angular velocity of a 3U CubeSat using μ PPTs with thruster allocation (right) under two thruster failure. 69

Figure 4-21: Pointing angle error of a 3U CubeSat using μ PPTs with paired firing (left) and thruster allocation (right) under three thruster failure. 69

Figure 4-22: Angular velocity of a 3U CubeSat using μ PPTs with paired firing (left) and thruster allocation (right) under three thruster failure. 70

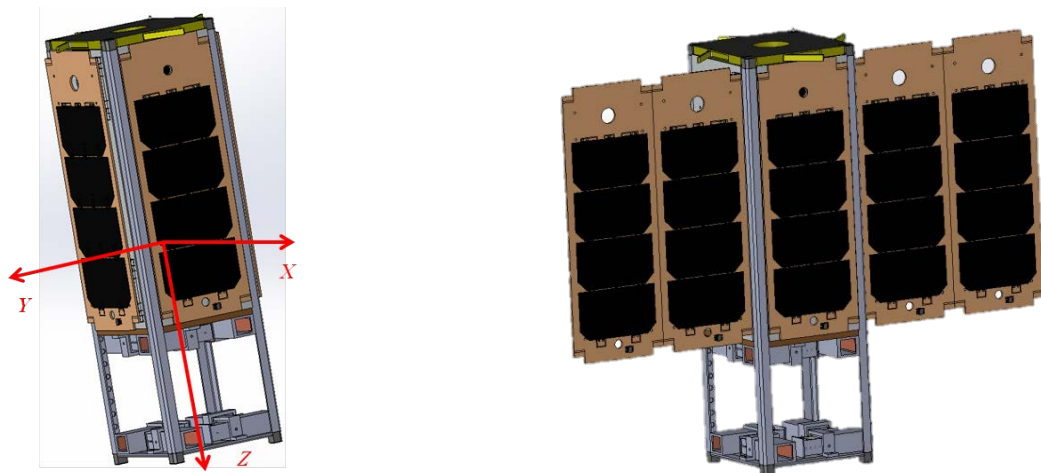
List of Tables

Table 1-1: ΔV and fuel mass budget for various missions	4
Table 2-1: CubeSat parameters for disturbance torque estimates	15
Table 3-1: Thruster pairs for paired firing method	39
Table 3-2: Performance comparison of control policies for pointing	46

Chapter 1.

Introduction

CubeSats have emerged as platforms for various low earth orbit (LEO) applications. Attitude control using propulsion requires the development of propulsive options that adhere to the physical constraints of CubeSats and provide the required impulse for typical LEO applications as well as novel implementation and development of suitable control approaches. The goal of this thesis is to investigate the performance of a 3U CubeSat design shown in Figure 1-1, with commercial-off-the-shelf (COTS) sensors and a 1U module of Teflon-fueled, micro-Pulsed Plasma Thrusters (μ PPT) for control functions including stabilization, pointing, and spinning. The CubeSat design is based on CubeSat mission studies at WPI (Major Qualifying Reports: NAG-1102, NAG-1204, NAG-1302, MAD-1101, MAD-1201, MAD-1301, JB3-CBS1, JB3-CBS2, JB3-CBS3). The μ PPT design and sizing was achieved by using simulations tools developed at WPI under a series of investigations on PPTs. (Gatsonis et al., 2001; Gatsonis et al., 2004; Gatsonis et al., 2007) The μ PPT design and Attitude Determination and Control (ADC) approach for CubeSats presented in this thesis and in Gatsonis et al. (2014) and Gatsonis et al. (2015) and can be applied to other nanosatellites (<10 kg) at LEO altitudes.



a). Surface mounted solar panel

b). Deployed solar panels expanded

Figure 1-1: A 3U CubeSat with the μ PPT module located in the bottom 1U.

1.1.Literature Review

Attitude control of CubeSats can utilize magnetic torquers, reaction wheels, control moment gyros, or propulsion systems (thrusters). Magnetic torquers are very popular due to their low mass, reliability and efficiency. The downside is that they cannot produce the large torques required for fast maneuvers with the power available (Roethlisberger et al., 2008; MAD-1101; MAD-1301; Visser, 2014). Reaction wheels can produce higher control torque output than magnetic torquers but they are more massive and can be less reliable over an extended lifetime due to the rotating wheels (Balan et al., 2008; Logan & Greenland., 2011). Rotation wheels are usually used in combination with magnetic torquers to provide wheel desaturation (Bridges et al., 2011; Hinkley & Hardy, 2012).

Propulsive options for attitude control of CubeSats are an emerging area and candidate technologies include cold gas and electric thrusters. A space propulsion system generates thrust

by accelerating a propellant mass at high velocity (Goebel & Katz, 2008). One measure for the efficiency of space propulsion system is the specific impulse (I_{sp}). With F designating the thrust force and \dot{m} the mass flow rate, the specific impulse is defined as

$$I_{sp} = \frac{\int_0^t F dt}{g \int_0^t \dot{m} dt} \quad (1.1)$$

where the numerator $\int_0^t F dt$ provides the impulse bit, I_{bit} . In cases where the thrust and mass flow rate are constant, Eq. (1.1) becomes

$$I_{sp} = \frac{F}{g\dot{m}} = \frac{V_e}{g} \quad (1.2)$$

The above expression shows that the average exit velocity of the ejected propellant, V_e is directly related to the thrust and mass flow rate. The relation between the mass of satellite, m , mass of fuel, m_f , specific impulse, I_{sp} , and ΔV is governed by well-known as the rocket equation

$$\Delta V = I_{sp} g \ln \left(\frac{m}{m - m_f} \right) \quad (1.3)$$

Table 1-1 lists ΔV estimates from Wertz & Larson (2008) Chapter 6 and the required fuel mass for typical orbital and attitude maneuvers on a CubeSat with total $m = 4$ kg and a propulsion system with $I_{sp} = 100$ s (typical for cold gas system) and $I_{sp} = 1000$ s (typical for electric propulsion), and $g = 9.8 \text{ m/s}^2$. The fuel mass requirement with cold gas is an order of

magnitude larger than that with EP and it is nearly impossible to perform inclination change with a cold gas system.

Table 1-1: ΔV and fuel mass budget for various missions

Types of Maneuver	Est. ΔV (m/s)	Fuel mass with Cold Gas (g)	Fuel mass with EP (g)
Coarse Attitude Maintenance	10-30	41-121	4-12
Altitude raising from 400 to 1000km	300	1054	121
De-orbiting from LEO to earth	500-2000	1600-3480	199-738
Change inclination in LEO			
by $\Delta\theta = 30^\circ$	4000	3932	1341
by $\Delta\theta = 60^\circ$	11000	~3999	2698

The main consideration in implementing propulsion system on CubeSats is the limitations due to volume, mass, and power available. Chemical thrusters have not been considered for CubeSat applications so far. Cold gas systems have low specific impulse and high volume/mass ratio but due to their simplicity and reliability have been considered in several CubeSat studies. Cold gas micro-propulsion with mass of 0.509 kg, thrust of 55 mN, specific impulse of 65s and total impulse of 34 N·s was considered for aerodynamic drag compensation on a CubeSat (Conklin et al. 2012). Delfi-n3Xt, a 3U CubeSat launched in 2013 was carrying a cold-gas micro-propulsion system with a thrust of 6 mN and specific impulse I_{sp} of 30s to maintain its orbit (Jong et al., 2008). The use of a highly miniaturized propulsion system (e.g. cold gas thruster) to demonstrate relative motion control between two CubeSats was investigated by Sundaramoorthy et al. (2010).

Electric thrusters provide high specific impulse but have low thrust. Electro-thermal thrusters such as the resistojet and arcjet produce thrust through gas dynamic acceleration of a gas that has been heated electrically. Ion, Hall, field emission electric propulsion (FEEP), and electrospray thrusters produce thrust primarily through electrostatic forces. Pulsed plasma thrusters (PPTs), vacuum arc thruster, and magnetoplasmadynamic (MPD) thrusters produce thrust primarily through electromagnetic forces. The PPT which is considered in this thesis generates thrust by ablating and ionizing a solid Teflon propellant through an electric discharge and then accelerates the plasma using a combination of Lorentz force and natural gas dynamic forces. Earlier PPTs employed in the Lincoln Experimental Satellite series (LES-6, LES-8/9) or the EO1 utilized parallel plate configurations (see references in Gatsonis et al. (2001)). Coaxial PPTs and μ PPTs have been considered as well (see references in Laperriere et al. (2005) and Shaw (2011)). The advantages of PPTs are the high specific impulse (over 1000s) and simple propellant management. There have been a number of applications of electric propulsion on CubeSats which involve resistojets, ion thrusters and PPTs which are reviewed below.

A resistojet with propellant mass of 0.6 kg, I_{sp} of 67-890s, and a volume of 1U, was considered by Moore et al. (2010) for the 2U RAMPART CubeSat. A propulsion module with eight μ PPTs for yaw, pitch and roll control was considered by Shaw and Lappas (2011) on STRaND-1, a 3U CubeSat. The propulsion module has a total mass of 0.34 kg with each μ PPT producing an impulse bit I_{bit} of 0.56 μ Ns and specific impulse of over 300s. Due to the limited control authority of this module, the final design removed thrusters for attitude control, and only a cold gas system was integrated for orbit control. Clark et al. (2011) evaluated the performance requirement of μ PPT with 0.3U and 150g mass for drag compensation and orbit maintenance. The UWE-4 Picosatellite is the first to incorporate vacuum arc thrusters to control the CubeSat's

orbit. The total propulsion system mass is only 0.2 kg, the impulse bit is 0.01 - 0.1 μNs , and the maximum pulse frequency is 20 Hz (Kronhaus et al., 2013). Conversano and Wirz (2013) have assessed the mission capability of CubeSats using a miniature ion thruster. They showed that depending on the thruster and propellant available, the ΔV can range from 1000 m/s to over 7000 m/s, enabling low-Earth-orbit inclination changes and even lunar missions.

In Gatsonis et al. (2014), a feasibility study is presented for using μPPTs on a 3U CubeSat to perform attitude control to meet pointing requirements at altitudes between 400 and 1000 km. The orbits and attitude control are consistent with science missions for ionospheric and solar observations. The positioning of the thrusters is such that they provide full, three-axis rotational control while maximizing the efficiency of each pulse. The aerodynamic, magnetic, solar radiation, and gravity gradient disturbance torques are included in the formulation. The study involves realistic power constraints anticipated on the 3U CubeSat. The paper introduces the control strategy based on a paired firing method and presents numerical simulation results for stabilization, pointing and spinning applications. In Gatsonis et al. (2015) the the CubeSat and mission design was further developed as well as the μPPT sizing analysis which in addition to compensation of disturbance torques includes stabilization (detumbling, spinning and de-spinning) and slew (pointing) maneuvers. An attitude determination and estimation method, sensor models was introduced followed by an improved attitude control approach which includes a thruster allocation method for robustness in place of the paired firing followed Gatsonis, et al. (2014).

1.2. Objectives and Approach

This thesis follows Gatsonis et al. (2014, 2015) and presents the overall design of a 3U CubeSat equipped with commercial-off-the shelf hardware, Teflon-fueled micro-Pulsed Plasma Thrusters (μ PPT), and an attitude determination and control (ADC) system. The objectives and approaches are:

- Use a 3U CubeSat design developed over a series of projects at WPI with commercial-off-the-shelf (COTS) sensors operating in LEO altitudes between 400 and 1000 km.
- Evaluate the disturbance torques experienced by 3U CubeSat for LEO applications using the CubeSat structure presented and analytical models for gravity,
- Evaluate the angular momentum required to perform stabilization of up to 20 deg/s and slew maneuvers of up to 180 degrees.
- Size the μ PPT by the impulse bit and pulse frequency required for various maneuvers. Use the ablation model (Gatsonis et al., 2007) and a performance model (Laperriere et al., 2005) to validate the practicality of the required size of μ PPT.
- Develop an attitude determination and estimation method for a CubeSat equipped with magnetometer, gyroscope, sun sensors, and GPS receivers (NAG-1204, MAD-1301, JB3-CBS3). Attitude determination is achieved through a q-method which uses pairs of the spacecraft-sun and the magnetic field vectors, one in the inertial reference frame and one in the body frame of the CubeSat. The attitude estimation implements in novel way approaches found on (Wie, 2008; Sidi, 2000; Markley & Crassidis, 2015). The

quaternion estimate and the gyroscope measurements are used with an extended Kalman filter to obtain the attitude estimates.

- Develop control methods for the 3U CubeSat with a μ PPT module as the actuator. Two control methods are developed: paired firing method, which is tailored to the specific thruster arrangement, and separate control algorithm and thruster allocation, which uses proportional and derivative control algorithms to calculate the torque required to compensate for the disturbance torques and to achieve specified stabilization and slewing maneuvers or combinations. The controller includes a thruster allocation approach which finds the optimal utilization of the available thrusters.
- Implement the ADC method in a simulation code based on MATLAB. In attitude determination, weight for sensor measurements needs to be chosen and in attitude estimation, covariance matrices have to be determined. Proper implementation in simulation is critical to obtain the correct results.
- Perform simulations for stabilization from 5 deg/s, pointing maneuvers for solar observation, and spinning up to 3 deg/s while maintaining pointing accuracy. Validate the control methods developed and validate the μ PPT sizing.

The Thesis is organized as follows: Chapter 2 presents the CubeSat design and thruster requirements; Chapter 3 presents the attitude dynamics, attitude estimation and control methods; Chapter 4 presents the simulation results for various mission scenarios; Chapter 4 summarizes the results and offers recommendations for future work.

Chapter 2.

CubeSat Design and Thruster Requirements

A CubeSat has very limiting volume, mass, and power constraints. For a 3U CubeSat, the volume is $10\text{cm} \times 10\text{cm} \times 30\text{cm}$ and the maximum mass is 4kg. The power is constrained by the overall design of the CubeSat (i.e. the number of solar panels). The design of the CubeSat in this study utilizes COTS hardware and an innovative μ PPT module for attitude control. In this chapter, the overall design of a 3U CubeSat is discussed in section 2.1 in order to meet the volume and mass limit, and later in the results section, issues related to power are addressed. In section 2.2, some useful reference frames for both attitude determination and attitude control are introduced. In section 2.3, the thruster requirement (i.e. impulse bit and pulse frequency) for disturbance torque compensation, stabilization, and slew maneuvers are discussed. Then in section 2.4, the design of the μ PPT, and its performance characteristics are introduced.

2.1. CubeSat Configuration

The baseline configuration of the 3U CubeSat considered is shown in Figure 1-1. The CubeSat is equipped with a magnetometer, a gyroscope, a GPS receiver, and five sun sensors as shown in Figure 2-1 for attitude determination. The CubeSat has an electrical power subsystem, power distribution module, battery board, and onboard computer. The bottom 1U is devoted to the thruster module with eight μ PPTs for attitude control. Two options for ADC are shown in

Figure 1-1, one with surface-mounted solar panels and the second with deployable solar panels, where the latter will be investigated in this thesis.

The μ PPT propulsion module shown in Figure 1-1 is designed to provide 3-axis control for a 3U CubeSat. It consists of 8 rectangular-geometry μ PPTs arranged in two layers. Each μ PPT includes a miniature spark igniter which creates a conductive path to initiate the primary discharge. This primary discharge has a period of τ_p then ablates and ionizes the Teflon to form the plasma that is accelerated with electromagnetic and gas dynamic forces.

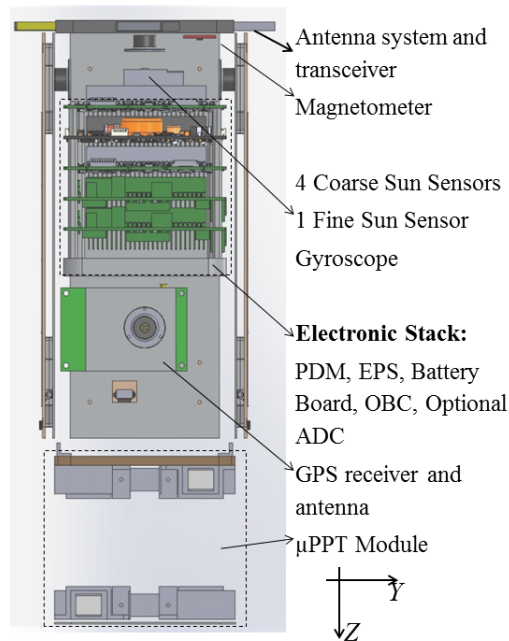
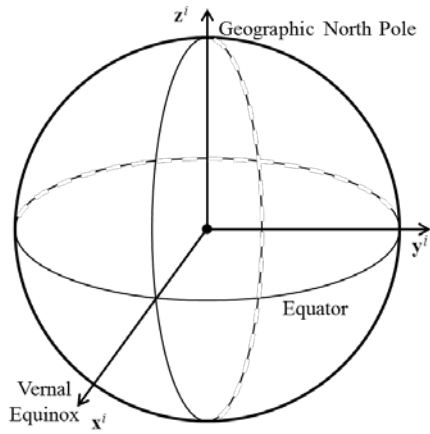


Figure 2-1: The 3U CubeSat with sun sensors are placed on +Y, -Y, -X and -Z faces.

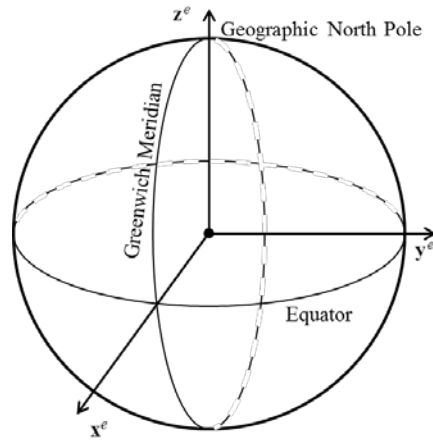
2.2. Reference Frames

The design of the CubeSat, sensor modeling, and implementation of the dynamics and attitude control method, requires the use of five reference frames: the Earth Centered Inertial (ECI), the Earth-Centered Earth-Fixed (ECEF), the Body Reference Frame (BRF), the Mission Reference

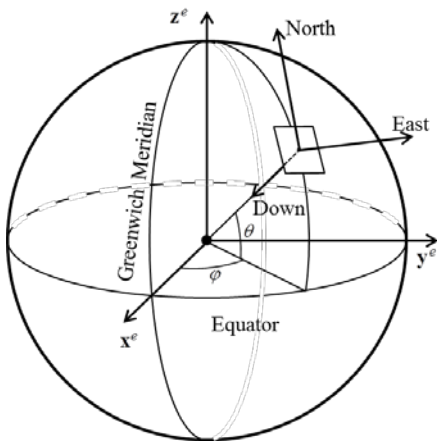
Frame (MRF) and the North-East-Down (NED) frame. The ECI frame shown in Figure 2-2a, is inertial and is best for describing the orbital motion of the satellite. The (ECEF) shown in Figure 2-2b is a rotating frame with referenced to a fixed point on the surface of the Earth. It is used by the Global Positioning System (GPS). The NED reference frame shown in Figure 2-2c is used in the International Geomagnetic Reference Field (IGRF) model. The BRF shown Figure 1-1 has its origin coincident with the center of mass of the CubeSat and is primarily used for sensor measurements, and actuator output. The X -axis is in the direction of the normal to the solar panels when they are fully deployed, the Z -axis is placed along the minor axis of inertia. The MRF shown in Figure 2-2d is mission-specific. In this study where sun pointing is of interest, the Z -axis is defined to be oriented along the direction of the Sun (or other targets), with the Y -axis orthogonal to the Z -axis and nadir direction.



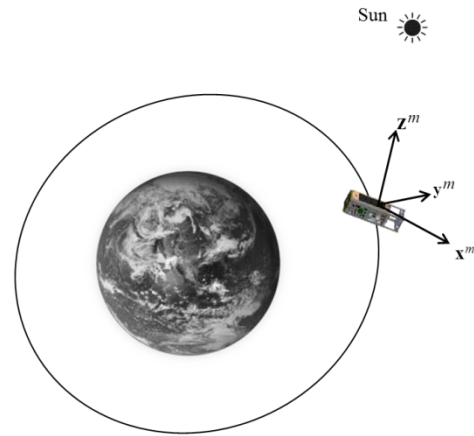
a). ECI reference frame.



b). ECEF reference frame.



c). NED reference frame.



d). MRF reference frame

Figure 2-2: Reference frames used in model, control and analysis.

2.3. Thruster Requirements for Disturbance Torques Compensation, Stabilization and Slew Maneuvers

2.3.1. Angular Momentum Evaluation

The μ PPT sizing (impulse bit and pulse frequency) requires evaluation of angular momentum imparted from disturbance torques over a specified time and the evaluation of angular momentum needed for stabilization and slewing maneuvers. Four cases of angular momentum are considered: the H_{cdt} accumulated from maximum constant disturbance torques over a time Δt_{cdt} ; the H_{pdt} accumulated from periodic disturbance torques over time Δt_{pdt} ; H_{st} required for de-spinning or spinning up within Δt_{st} , for a change in angular velocity of $\Delta\omega$; and H_{sl} associated with a 180-degree slew maneuver over time Δt_{sl} with zero initial and final angular velocity.

CubeSats in LEO experience disturbance torques due to aerodynamic drag, gravity gradient, the magnetic field, and solar radiation (Wertz & Larson, 2008). The disturbance torque due to aerodynamic drag is described by

$$T_a = \frac{1}{2} \rho A C_D v^2 (c_{pa} - c_g), \quad (1.4)$$

where ρ is the background atmospheric density, A is the cross sectional surface area normal to the velocity vector, C_D is the drag coefficient, v is the speed of CubeSat, c_{pa} is the center of aerodynamic pressure, and c_g is the center of mass. The gravitational torque is due to the

variation of the gravitational force over the CubeSat. Assuming a spherical mass distribution for the Earth, the gravitational torque is given by Wertz & Larson (2008)

$$T_g = \frac{3\mu}{2r^3} |I_z - I_y| \sin(2\theta), \quad (1.5)$$

where $\mu = 3.986 \times 10^5 \text{ km}^3 \cdot \text{s}^{-2}$ is the Earth's gravity constant, r is orbit radius (km), β is the maximum deviation of the Z-axis in Figure 1-1b relative to a nadir pointing vector in radians, and I_z and I_y are the minor moments of inertia. The solar radiation torque is given by Wertz & Larson (2008)

$$T_{sp} = \frac{F_s}{c} A_s \cos(i) (1 + q_r) (c_{ps} - c_g), \quad (1.6)$$

where $F_s = 1367 \text{ W/m}^2$ is the incident solar radiation constant, c is the speed of light, A_s is the surface area, c_{ps} is the location of the center of solar pressure, c_g is the center of mass, q_r is the reflectance factor and i is the angle of incidence of the Sun relative to X-axis in Figure 1-1, ($i = 0$ if the sunlight is aligned with X-axis). Finally, the magnetic torque from the interaction between the Earth's geomagnetic field and the satellite's residual magnetic dipole moment is given by Wertz & Larson (2008)

$$T_m = D \frac{2M}{r^3}, \quad (1.7)$$

where $M = 7.96 \times 10^{15} \text{ T} \cdot \text{m}^3$ is the magnetic moment of the Earth, D is the residual magnetic dipole moment generated by onboard instruments and current-carrying wires, and is estimated based on the mass of CubeSat, M_c as $D = M_c \times 0.001 \text{ A} \cdot \text{m}^2 / \text{kg}$ (Wertz, 1980).

For evaluation of the maximum torques, 3U CubeSat shown in Figure 1-1b with its solar panels fully deployed is considered, the velocity $v = \sqrt{\mu/r}$ is assumed to be in the direction normal to the solar panels, and input parameters are shown in Table 2-1. The aerodynamic torque is evaluated for maximum and minimum solar activity conditions. Figure 2-3 shows the disturbance torques as a function of altitude. The aerodynamic drag is evaluated for maximum and minimum solar activity conditions. At altitudes above 500 km the maximum disturbances are due to solar pressure and magnetic field while at altitudes below 400 km the aerodynamic torque becomes dominant. At an altitude of 400 km, the maximum disturbance torque is $T^{\max} = 6 \times 10^{-6} \text{ N} \cdot \text{m}$.

Table 2-1: CubeSat parameters for disturbance torque estimates

Parameters	Values
C_D	3
A	0.07 m ²
$c_{pa} - c_g$	0.05 m
β	30 deg
$I_z - I_y$	0.025 kg · m ²
A_s	0.07 m ²
$c_{ps} - c_g$	0.05 m
q_r	1
i	0 deg
D	0.004 A · m ²

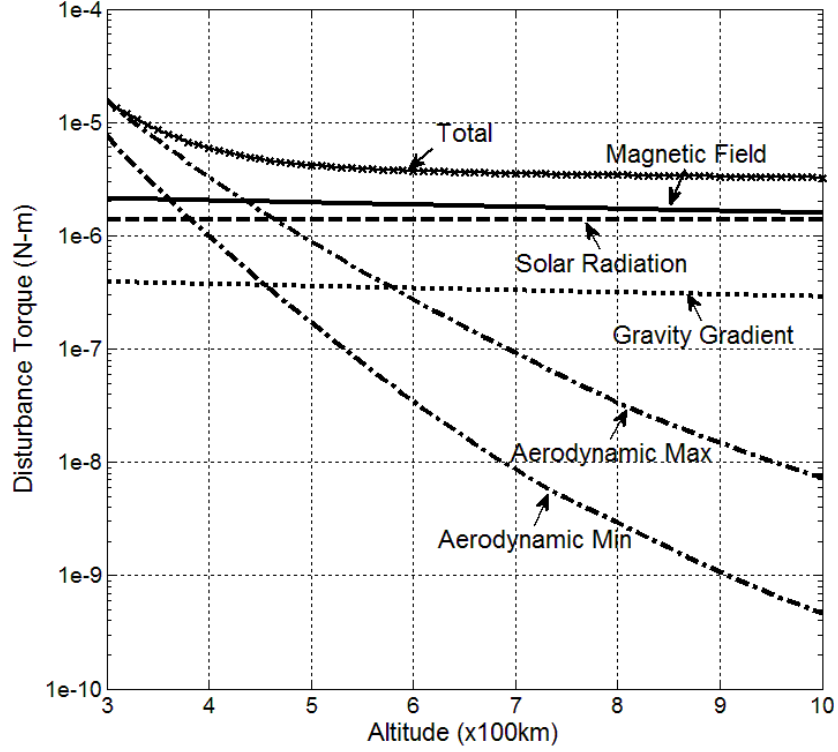


Figure 2-3: Disturbance torques on a 3U CubeSat at altitudes from 300 to 1000 km.

The maximum constant angular momentum accumulated over an arbitrary time Δt_{cdt} due to the maximum disturbance torque T^{\max} is

$$H_{cdt} = T^{\max} \Delta t_{cdt} \quad (1.8)$$

The periodic angular momentum accumulated over time Δt_{pdt} due to disturbance torques with period P is

$$H_{pdt} = \int_0^{\Delta t_{pdt}} |T(t)| dt = \int_0^{\Delta t_{pdt}} \left| T^{\max} \cos\left(\frac{2\pi}{P}t\right) \right| dt \quad (1.9)$$

The absolute value sign is used to calculate the accumulated angular momentum magnitude and the disturbance torque is continuously compensated over the time period of interest. Consider a time such that Δt_{pdt} is an integer multiple of P , then Eq. (1.9) can be rewritten as:

$$H_{pdt} = \frac{\Delta t_{pdt}}{P} 2 \int_0^{P/2} T^{\max} \cos\left(\frac{2\pi}{P}t\right) dt = T^{\max} \frac{\Delta t_{pdt}}{\pi} \quad (1.10)$$

The angular momentum required for stabilization or spinning up with a change in angular velocity of $\Delta\omega$ is

$$H_{st} = I|\Delta\omega|, \quad (1.11)$$

For slew maneuvers, $\omega_i = \omega_f = 0$ deg/s, Δt_{sl} is the required slew time, and the idle period (i.e. the amount of time when the thrust is not applied) is $\alpha\Delta t_{sl}$ as shown in Figure 2-4.

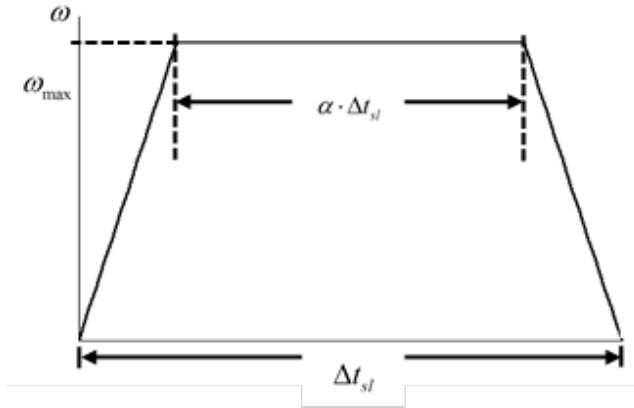


Figure 2-4: Illustration for slew maneuver with definition of idle period.

The angular velocity ω_{\max} needed to be achieved

$$\Delta\theta = \alpha \cdot \Delta t_{sl} \cdot \omega_{\max} + \frac{1}{2}(1-\alpha) \cdot \Delta t_{sl} \cdot \omega_{\max}, \quad (1.12)$$

$$\omega_{\max} = \frac{2\Delta\theta}{(1+\alpha)\Delta t_{sl}}.$$

Then the angular momentum required for such a slew maneuver is

$$H_{sl} = I \left(|\omega_{\max} - \omega_0| + |\omega_{\max} - \omega_f| \right) = \frac{4I\Delta\theta}{(1+\alpha)\Delta t_{sl}}. \quad (1.13)$$

2.3.2. Impulse Bit and Pulse Frequency Requirements

The μ PPT considered in this investigation has a rectangular geometry and uses solid Teflon as a propellant. Each pulse has a duration τ_p which is assumed to be equal to the duration of the primary capacitor discharge. The firing (or thrust or pulse) period is t_p , the pulse frequency is $f_p = t_p^{-1}$ and the duty cycle expressed as the percentage of one period in which thrust is produced $D = (\tau_p / t_p)100\%$. The duration of N_p pulses, i.e. total on-time when the thrust is produced, is

$$\tau = N_p \cdot \tau_p, \quad (1.14)$$

and the total firing (or thrust) time which includes the on-time and off-time is ,

$$t = N_p \cdot t_p = N_p \frac{1}{f_p}. \quad (1.15)$$

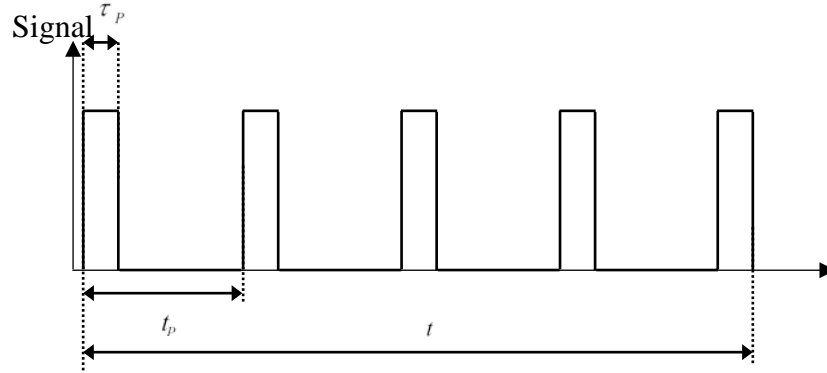


Figure 2-5: Diagram representing idealized, thrust vs. time profile for a PPT pulse train

For thruster sizing purposes, the required impulse bit I_{bit} ($\mu\text{N} \cdot \text{s}$) and pulse frequency f_p (Hz) for the μPPT are to be determined. For an angular momentum H to be delivered by a thruster with moment arm of s the number of pulses per thruster is

$$N_p = \frac{H}{n \cdot I_{bit} \cdot s}, \quad (1.16)$$

where n is the number of thrusters in one of the six directions (positive x , y , z , and negative x , y , z direction). The thruster has the property of providing unilateral control reaction which means that the thruster providing torque in the positive x direction can only produce torque in the positive x direction. For attitude control at least one thruster is needed for one of the six directions and six thrusters are required to maintain full control over three axes. Note that thrust forces are not acting as balanced couples, and some translational motion is expected, but such motion is small enough to be neglected. The required firing time can be obtained using Eq. (1.15) and rewrite Eq. (1.16) as

$$t = \frac{H}{f_P \cdot n \cdot I_{bit} \cdot s} \quad (1.17)$$

By introducing the average angular momentum rate $\dot{H} = H / t$, the above can be written as

$$f_P \cdot I_{bit} \cdot n \cdot s = \dot{H} \quad (1.18)$$

which relates the thruster design parameters I_{bit} , and f_P , the CubeSat design characteristics n , and s to the mission requirement \dot{H} (or H derived earlier over the desired firing time t).

For a constant disturbance torque, if compensation is achieved continuously over a firing time of $t = \Delta t_{cdt}$ then

$$\dot{H}_{cdt} = T^{\max} \quad (1.19)$$

For periodic disturbance torque, if compensation is achieved over a time period of $t = \Delta t_{pdt}$ then

$$\dot{H}_{pdt} = \frac{T^{\max}}{\pi}. \quad (1.20)$$

For stabilization or spinning, $t = \Delta t_{st}$ and therefore,

$$\dot{H}_{st} = \frac{I|\Delta\omega|}{\Delta t_{st}}. \quad (1.21)$$

For the slew maneuver, the firing time $t = (1 - \alpha)\Delta t_{sl}$ and

$$\dot{H}_{sl} = \frac{4I\Delta\theta}{(1-\alpha^2)\Delta t_{sl}^2}. \quad (1.22)$$

For a 3U CubeSat with thrusters located as shown in Figure 1-1a, the moment arm has value from 3 cm to 20 cm. The assumptions for sizing purposes are $s = 0.14$ m and that there is only one μ PPT in each direction, $n = 1$. For a given maneuver and time duration, the angular momentum rate is found using Eq. (1.19), (1.20), (1.21), and (1.22), and plotted in Figure 2-6. Then, Eq. (1.18) is used to provide bounds on the required I_{bit} and f_p of the μ PPT which are plotted in Figure 2-7.

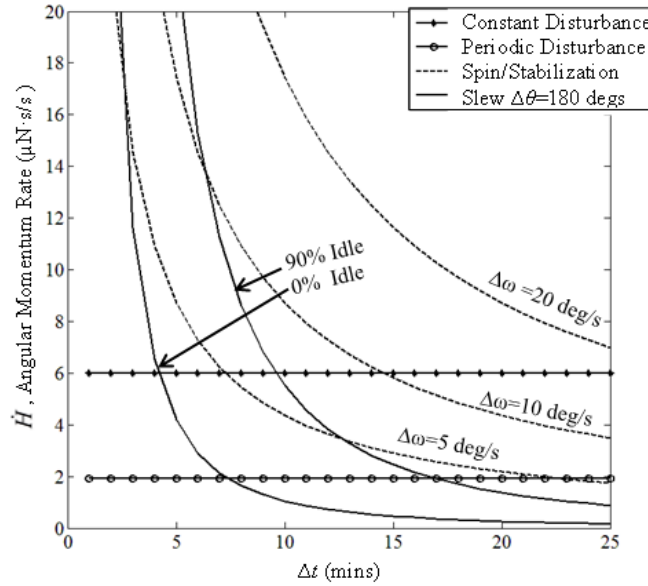


Figure 2-6: Angular momentum rate \dot{H} for different maneuvers of a given duration.

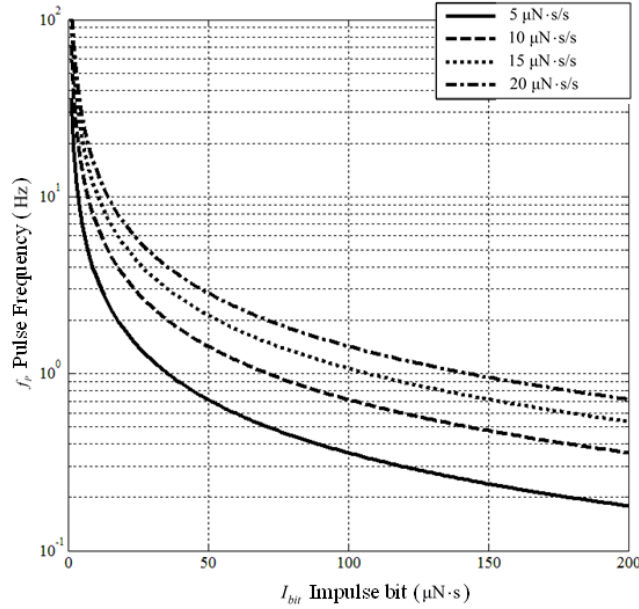


Figure 2-7: Requirement of impulse bit and pulse frequency at different angular momentum rate

2.4. μ PPT Design

The rectangular μ PPT can be accommodated within the available volume in the 3U CubeSat and is sized to provide the required impulse bit. The propulsion module, consisting of thrusters, fits in a 1U volume of a CubeSat. The design and performance characteristics (I_{sp} , I_{bit}) of the μ PPT are derived in an iterative procedure using the performance model of Laperriere et al. (2005) with the ablation model of Gatsonis et al. (2007). The performance model includes inputs which incorporate several design features of a rectangular μ PPT (e.g. height of channel, discharge time, and electrical characteristics of the electrodes). The ablation model is used to provide the ablation profile using as inputs the geometrical characteristics of the Teflon bar, pulse duration and material properties. Using these two models, a μ PPT and propulsion module is purposed, as shown in Figure 2-8. The thruster consists of two parallel electrodes with length

of 3.25 cm and width of 1.25 cm. These tungsten coated copper electrodes are 0.75 cm thick, 1.5 cm apart and are housed in a Torlon casing as shown in Figure 2-8. This μ PPT design can provide I_{bit} (10- 80 $\mu\text{N}\cdot\text{s}$) with input energy below 1.5 J per pulse and operate over the range of pulse frequency f_p shown in Figure 2-7.

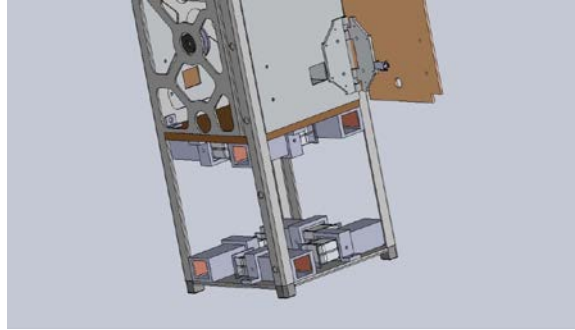


Figure 2-8: Bottom 1U of CubeSat showing the thrusters comprising the μ PPT module.

Chapter 3.

Attitude Dynamics, Estimation and Control

Attitude determination is the process of calculating the orientation of the spacecraft relative to a reference frame or an object of interest. The accuracy of attitude determination is bounded by the accuracy of sensors and quality of the algorithms utilized. Attitude estimation is the process of predicting the future orientations of the spacecraft based on a dynamic model and using previous information on the the spacecraft's attitude. With the increasing onboard computational power attitude estimation has becomes essential part of an ADC system.

In this chapter, the continuous-time dynamic model of the spacecraft is developed in section 3.1 and the attitude determination and estimation method is introduced. In section 3.2, davenport's q-method is discussed and the reference models and sensors models are introduced which are used for attitude determination. In section 3.3, the attitude estimation algorithm known as extended Kalman filter is presented. In section 3.4, a dynamics model for thruster and its control implementation are developed. Two attitude control method are also developed and discussed: paired firing, and separate control algorithm and thruster allocation. Thruster allocation methods usually appear as an optimization problem and are utilized in over-actuated system (Oppenheimer & Doman, 2006).

3.1. Attitude Dynamics and Estimation

The 3U CubeSat is modeled as a rigid body and its attitude dynamics is expressed via Euler's equation in terms of the angular velocity, $\boldsymbol{\omega}(t) = (\omega_x(t), \omega_y(t), \omega_z(t))$, the disturbance torques, $\mathbf{T}_D(t)$, the control torque, $\mathbf{T}_C(t)$, and the inertia matrix \mathbf{I} (Wie 2008) :

$$\mathbf{I}\dot{\boldsymbol{\omega}}(t) = [\mathbf{T}_C(t) + \mathbf{T}_D(t) - (\boldsymbol{\omega}(t) \times \mathbf{I}\boldsymbol{\omega}(t))]. \quad (2.1)$$

The differential equations for quaternion kinematics $\mathbf{q}(t)$ is given by:

$$\dot{\mathbf{q}}(t) = \frac{1}{2}\boldsymbol{\Omega}(\boldsymbol{\omega}(t))\mathbf{q}(t) = \frac{1}{2} \begin{bmatrix} 0 & \omega_z(t) & -\omega_y(t) & \omega_x(t) \\ -\omega_z(t) & 0 & \omega_x(t) & \omega_y(t) \\ \omega_y(t) & -\omega_x(t) & 0 & \omega_z(t) \\ -\omega_x(t) & -\omega_y(t) & -\omega_z(t) & 0 \end{bmatrix} \mathbf{q}(t) . \quad (2.2)$$

Attitude estimation is implemented in this study as a two-step process following established approaches (Markley & Crassidis, 2015; Wertz, 1980) as shown in Figure 3-1: the reference models (calculated vectors), attitude determination and estimation will be performed in real time on the spacecraft whereas the plant (dynamic equations) and simulated measurement will be part of the simulation. Note that orbital state data is not propagated in this study, the position data is preloaded from data evaluated using Systems Tool Kit (STK). The first step follows the q-method for static attitude determination in order to obtain an estimate of the quaternion denoted by $\mathbf{y}_q(t)$. The q-method uses pairs of the spacecraft-sun and the magnetic field vectors, one in the inertial reference frame and one in the body frame of the CubeSat. The second step uses the quaternion estimate $\mathbf{y}_q(t)$ and the gyroscope measurements denoted by $\mathbf{y}_G^b(t)$ with an Extended Kalman Filtering (EKF) algorithm to obtain the attitude estimates $\hat{\boldsymbol{\omega}}(t)$ and $\hat{\mathbf{q}}(t)$.

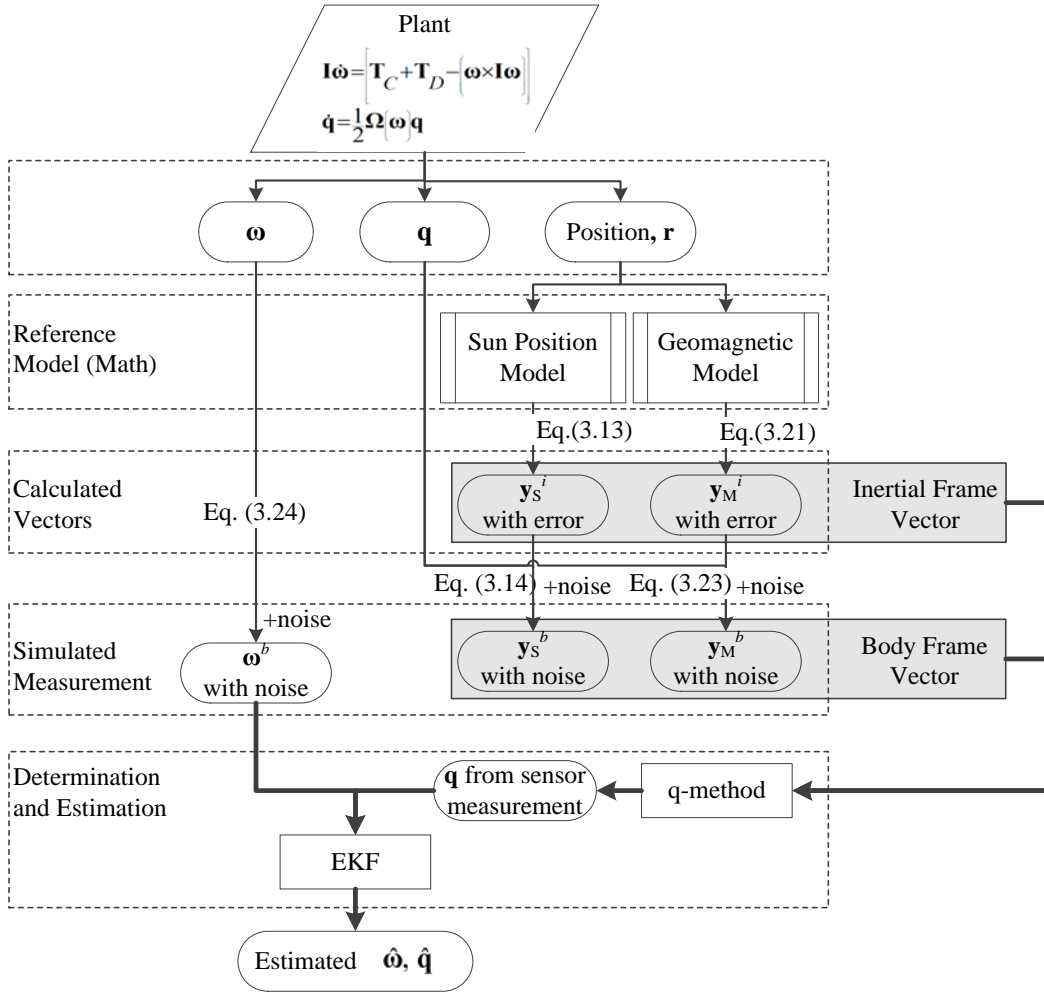


Figure 3-1: Flow chart for simulation, attitude determination and estimation.

3.2. Static Attitude Determination

3.2.1. Davenport's q-method

The q-method uses two or more sets of non-collinear vectors, one in the inertial reference frame and one in the body frame of the CubeSat to obtain the direction cosine matrix that relates the two frames. The body-fixed vector \mathbf{y}^b provides the measured directions by the on-board

sensors and the inertia-frame vector \mathbf{y}^i provides the directions from a reference (mathematical) model. The two directions are related by the rotational matrix \mathbf{A}^{bi} from ECI to BRF such that

$$\mathbf{y}^b = \mathbf{A}^{bi} \mathbf{y}^i + \delta \mathbf{y} \quad (2.3)$$

where $\delta \mathbf{y}$ is the error term which denotes errors from both sensor measurements and mathematical models. The attitude matrix \mathbf{A}^{bi} can be represented as (Wertz, 1980)

$$\mathbf{A}^{bi}(\mathbf{q}) = (q_4^2 - \|\mathbf{q}_{1:3}\|^2) \mathbf{I}_{3 \times 3} + 2\mathbf{q}_{1:3} \mathbf{q}_{1:3}^T - 2q_4 [\mathbf{q}_{1:3} \times] \quad (2.4)$$

where the quaternion $\mathbf{q} = [\mathbf{q}_{1:3}^T \quad q_4]^T$ with $\mathbf{q}_{1:3}$ its vector part and q_4 its scalar component, and $[\mathbf{q}_{1:3} \times]$ is the cross product matrix, defined by

$$[\mathbf{q}_{1:3} \times] \triangleq \begin{bmatrix} 0 & -q_3 & q_2 \\ q_3 & 0 & -q_1 \\ -q_2 & q_1 & 0 \end{bmatrix} \quad (2.5)$$

where q_i is the i th entry in the vector part of the quaternion. Wahba (1965) proposed a constrained least squares estimation for finding an orthogonal matrix \mathbf{A}^{bi} with determinant +1 using n measurements as

$$\min_{\mathbf{A}^{bi}} \sum_{j=1}^n \left\| (\mathbf{y}^b)_j - \mathbf{A}^{bi} (\mathbf{y}^i)_j \right\|^2 \quad \text{subject to } \det[\mathbf{A}^{bi}] = 1, \quad (2.6)$$

where $(\mathbf{y}^b)_j$ and $(\mathbf{y}^i)_j$, $j=1, \dots, n$, are the n unit vectors measured in the body and inertial frame, respectively. The above can be solved using the q-method with Eq. (2.4), represented as (Markley & Crassidis, 2015)

$$\frac{1}{2} \sum_{j=1}^n a_j \left\| \left(\mathbf{y}^b \right)_j - \mathbf{A}^{bi} \left(\mathbf{y}^i \right)_j \right\|^2 = 1 - \mathbf{q}^T \mathbf{K} \mathbf{q}, \quad (2.7)$$

where $\{a_j\}$ are non-negative weights, assumed for simplicity to be equal to $1/n$. The optimal K is evaluated through the set of measured (body-frame) and reference (inertia-frame) vectors

$$K \triangleq \begin{bmatrix} \mathbf{S} - I_{3 \times 3} \text{tr}(\mathbf{D}) & \mathbf{N} \\ \mathbf{N}^T & \text{tr}(\mathbf{D}) \end{bmatrix} \quad (2.8)$$

where

$$\mathbf{S} = \mathbf{D} + \mathbf{D}^T, \quad \mathbf{D} = \sum_{j=1}^n a_j \left(\mathbf{y}^b \right)_j \left[\left(\mathbf{y}^i \right)_j \right]^T, \quad \mathbf{N} = \sum_{j=1}^n a_j \left(\left(\mathbf{y}^b \right)_j \times \left(\mathbf{y}^i \right)_j \right). \quad (2.9)$$

The optimal quaternion estimate using Davenport's q-method is given by

$$\mathbf{y}_q = \mathbf{q}_{\max} \quad (2.10)$$

where \mathbf{q}_{\max} is the normalized eigenvector corresponding to the largest eigenvalue of K in Eq. (2.8). Other methods have been developed later based on davenport's q-method, some of which utilizes numerical methods to solve the eigenvector problem. Modern attitude determination methods are primarily a variation of q-method and are designed to meet specific mission requirements.

3.2.2. Sensors and Reference Models

The reference models used provide the Sun position (ECI) and the geomagnetic field (NED). The onboard sensors provide the sun vector (BRF), the magnetic field vector (BRF), the angular

velocity (BRF), position, and velocity (ECEF) and are modeled for software implementation in this study.

3.2.2.1. Sun Vector in the Body Frame and Inertial Frame

Sun sensors onboard the CubeSat provide either one-axis or two-axis information in the BRF. A sun-sensor model is introduced here using two-axis information, α and β as the true angles measured from the sun sensor. The orientation of the sun sensor in BRF affects the sun vector calculation. To illustrate this procedure, sun sensor mounted on the surface of positive Z-axis is taken as an example (α and β represent the sun angle relatively to X- and Y- axis respectively):

$$\begin{aligned} \tilde{\mathbf{y}}_S^{b,true} &= \begin{bmatrix} \tan \alpha \\ \tan \beta \\ 1 \end{bmatrix}, & \mathbf{y}_S^{b,true} &= \frac{\tilde{\mathbf{y}}_S^{b,true}}{\|\tilde{\mathbf{y}}_S^{b,true}\|}, \\ \tilde{\mathbf{y}}_S^b &= \begin{bmatrix} \tan(\alpha + v_{S,\alpha}) \\ \tan(\beta + v_{S,\beta}) \\ 1 \end{bmatrix}, & \mathbf{y}_S^b &= \frac{\tilde{\mathbf{y}}_S^b}{\|\tilde{\mathbf{y}}_S^b\|} \end{aligned} \tag{2.11}$$

where $v_{S,i}$ is a scalar Gaussian noise with zero mean.

The reference model for the position of the Sun in the ECI frame is derived from HM Nautical Almanac Office (2010) which set the Julian date of 1/1/2000 as the reference date for the sun position. The mean longitude of the Sun, L , mean anomaly, g , ecliptic longitude, λ , obliquity (axial tilt) of the ecliptic, ε , and distance of the Sun from the Earth, r_s , are calculated from the following equations where all the angles are expressed in degrees and distances in astronomical units

$$\begin{aligned}
L &= 280.460^\circ + 0.9856474^\circ JD_{2000} \\
g &= 357.528^\circ + 0.9856003^\circ JD_{2000} \\
\lambda &= L + 1.915^\circ \sin(g) + 0.020^\circ \sin(2g) \\
\varepsilon &= 23.439^\circ - 0.0000004^\circ JD_{2000} \\
r_s &= 1.00014 - 0.01671 \cos(g) - 0.00014 \cos(2g)
\end{aligned} \tag{2.12}$$

Then the position of the Sun in the ECI frame is given by

$$\begin{aligned}
y_{S,x}^i &= r_s \cos(\lambda) \\
y_{S,y}^i &= r_s \cos(\varepsilon) \sin(\lambda) \\
y_{S,z}^i &= r_s \sin(\varepsilon) \cos(\lambda)
\end{aligned} \tag{2.13}$$

The application of q-method is expressed as

$$\mathbf{y}_S^b = \mathbf{A}^{bi} \mathbf{y}_S^i + \mathbf{v}_S \tag{2.14}$$

To generate simulated sun-sensor data, the sun vector \mathbf{y}_S^i in the ECI frame by Eq. (2.13) is calculated which then is converted to the sun vector \mathbf{y}_S^b in BRF frame using Eq. (2.14). The simulated data are then obtained by reversing the calculation:

$$\begin{aligned}
\alpha &= \text{acos}(y_{S,1}^{b,true}) + v_{S,\alpha} \\
\beta &= \text{acos}(y_{S,2}^{b,true}) + v_{S,\beta}
\end{aligned} \tag{2.15}$$

3.2.2.2. Magnetic Field Vector in the Body Frame and Inertial Frame

The body-frame magnetic-field vector is provided by the onboard magnetometer as

$$\mathbf{y}_M^b = \mathbf{y}_M^{b,true} + \mathbf{v}_M \tag{2.16}$$

The inertial frame (ECI) magnetic-field vector is derived from the International Geomagnetic Reference Field (IGRF-11) model (Finlay et al., 2010) which provides the \mathbf{B} field in the NED frame. The governing equation for the magnetic induction in the IGRF model is

$$\mathbf{B}(r, \theta, \varphi, t) = -\nabla V \quad (2.17)$$

where V is a finite series having the numerical Gauss coefficients $g_n^m(t)$ and $h_n^m(t)$ (in nT)

$$V(r, \theta, \varphi, t) = a \sum_{n=1}^N \sum_{m=0}^n \left(\frac{a}{r}\right)^{n+1} \left[g_n^m(t) \cos(m\varphi) + h_n^m(t) \sin(m\varphi) \right] P_n^m(\cos(90^\circ - \theta)) \quad (2.18)$$

In the above expression, r is the radial distance from the center of the Earth (km), $a = 6371.2$ km is the magnetic reference spherical radius, θ is geocentric latitude (degrees), and φ is east longitude. $P_n^m(\cos \theta)$ are the Schmidt semi-normalized associated Legendre functions of degree n and order m . The Gauss coefficients $g_n^m(t)$ and $h_n^m(t)$ are provided for the main field at epochs separated by 5-year intervals between 1900 and 2010. The coefficients at a specific time can be found using linear interpolation

$$\begin{aligned} g_n^m(t) &= g_n^m(T_0) + \dot{g}_n^m(T_0)(t - T_0) \\ h_n^m(t) &= h_n^m(T_0) + \dot{h}_n^m(T_0)(t - T_0) \end{aligned} \quad (2.19)$$

The Schmidt Quasi-normalization function $P_n^m(\cos \theta)$ is provided in Winch et al. (2005) as

$$P_n^m(\mu) = \sqrt{2 \frac{(n-m)!}{(n+m)!}} (1-\mu^2)^{\frac{m}{2}} \left(\frac{d}{d\mu}\right)^m P_n(\mu) \quad (2.20)$$

The components of the geomagnetic field in the northward, eastward and radially inward directions are obtained with the following equations (HM Nautical Almanac Office, 2010)

$$\begin{aligned}
y_{M,x}^n &= \frac{1}{r} \frac{\partial V}{\partial \theta} = \sum_{n=1}^N \sum_{m=0}^n \left(\frac{a}{r} \right)^{n+2} \left[g_n^m(t) \cos(m\varphi) + h_n^m(t) \sin(m\varphi) \right] P_n^m(\sin(90^\circ - \theta)) \\
y_{M,y}^n &= \frac{1}{r \sin(90^\circ - \theta)} \frac{\partial V}{\partial \varphi} = -\frac{1}{\sin(90^\circ - \theta)} \sum_{n=1}^N \sum_{m=0}^n \left(\frac{a}{r} \right)^{n+2} \left\{ \begin{aligned} & \left[h_n^m(t) \cos(m\varphi) - g_n^m(t) \sin(m\varphi) \right] \\ & \times m P_n^m(\cos(90^\circ - \theta)) \end{aligned} \right\} \quad (2.21) \\
y_{M,z}^n &= \frac{\partial V}{\partial r} = \sum_{n=1}^N \sum_{m=0}^n (n+1) \left(\frac{a}{r} \right)^{n+2} \left[g_n^m(t) \cos(m\varphi) + h_n^m(t) \sin(m\varphi) \right] P_n^m(\cos(90^\circ - \theta))
\end{aligned}$$

The magnetic field vector in the ECI frame is obtained using the satellite's position in ECEF (longitude φ , and latitude θ) and \mathbf{y}_M^n , and an intermediate transformation matrix from ECEF to ECI, \mathbf{A}^{ei}

$$\mathbf{y}_M^i = \mathbf{A}^{ei} \begin{bmatrix} \cos \varphi & -\sin \varphi & 0 \\ \sin \varphi & \cos \varphi & 0 \\ 0 & 0 & 1 \end{bmatrix} \begin{bmatrix} -\sin \theta & 0 & \cos \theta \\ 0 & 1 & 0 \\ -\cos \theta & 0 & \sin \theta \end{bmatrix} \mathbf{y}_M^n \quad (2.22)$$

To generate simulated magnetometer data in the BRF, Eq. (2.22) is used to obtain the magnetic field vector in the ECI frame, which is then converted into the BRF frame using

$$\mathbf{y}_M^b = \mathbf{A}^{bi} \mathbf{y}_M^i + \mathbf{v}_M \quad (2.23)$$

where \mathbf{v}_M is a randomly generated 3×1 noise vector with Gaussian distribution with zero mean.

The observations in (2.14) and (2.23) provide the measurements for the q-method, i.e. with $n = 2$ the two body frame measurements $\{\mathbf{y}_M^b, \mathbf{y}_S^b\}$ and the two inertial frame measurements $\{\mathbf{y}_M^i, \mathbf{y}_S^i\}$

are used in (2.8), (2.9), and (2.10) to obtain the estimate of the quaternion $\mathbf{y}_q(t)$ using the aforementioned static attitude determination method.

3.3. Attitude Estimation with Extended Kalman Filtering (EKF)

The next step is to find the best estimate of the true system using the dynamic model and measurements. The EKF provides the attitude estimates $\hat{\boldsymbol{\omega}}(t)$ and the quaternion estimate $\hat{\mathbf{q}}(t)$ using the (static) estimate of the quaternion $\mathbf{y}_q(t)$, the gyroscope measurements denoted by $\mathbf{y}_G^b(t)$, and the dynamic equations Eq. (2.1) and Eq. (2.2).

Rate gyroscopes provide the CubeSat's angular velocity in BRF frame. The gyroscope measurements, \mathbf{y}_G^b is given by

$$\mathbf{y}_G^b = \boldsymbol{\omega} + \mathbf{v}_G \quad (2.24)$$

where $\boldsymbol{\omega}$ is the true angular velocity and \mathbf{v}_G is the white noise (3×1) vector. To obtain simulated gyroscope data Eq. (2.24) is used where $\boldsymbol{\omega}$ is from Eq. (2.1) and \mathbf{v}_G is a randomly generated 3×1 noise vector with Gaussian distribution and zero mean.

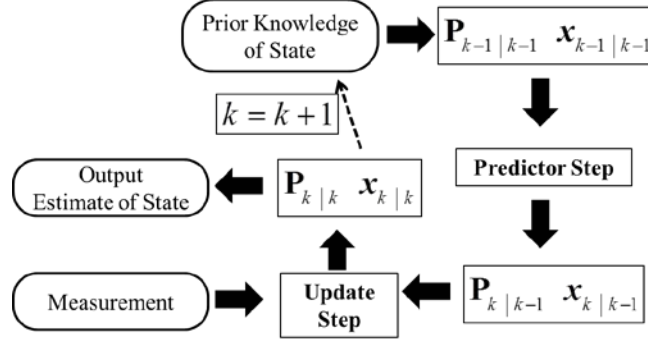


Figure 3-2: Outline for extended Kalman filter algorithm

Figure 3-2 shows the basic outline to implement the extended Kalman filter algorithm. Eq. (2.1) and Eq. (2.2) are rewritten in state-space form as

$$\begin{aligned} \dot{\mathbf{x}}(t) &= \begin{pmatrix} \dot{\boldsymbol{\omega}} \\ \dot{\mathbf{q}} \end{pmatrix} = \begin{pmatrix} \mathbf{I}^{-1} \mathbf{T}_C - \mathbf{I}^{-1} (\boldsymbol{\omega} \times \mathbf{I} \boldsymbol{\omega}) \\ \frac{1}{2} \boldsymbol{\Omega}(\boldsymbol{\omega}) \mathbf{q} \end{pmatrix} + \mathbf{w}(t) \\ \mathbf{y}(t) &= \begin{pmatrix} \boldsymbol{\omega} \\ \mathbf{q} \end{pmatrix} + \mathbf{v}(t) = \begin{pmatrix} \mathbf{y}_G \\ \mathbf{y}_q \end{pmatrix} \end{aligned} \quad (2.25)$$

where $\mathbf{w}(t)$ is a Gaussian process noise with covariance matrix \mathbf{Q} and zero-mean and $\mathbf{v}(t)$ is the Gaussian observation (sensor) noise with covariance matrix \mathbf{R} and zero mean. The covariance matrix \mathbf{R} is a square diagonal matrix with σ corresponding to gyroscope by the first three entries and σ of the sun sensors chosen as the last four entries. The covariance matrix \mathbf{Q} has to be tuned in order to achieve good EKF performance. Using the notation $G_k = G(k\Delta t)$ to denote the discrete-time representation of a quantity $G(t)$, the discrete-time state-space representation of Eq. (2.25) is

$$\begin{aligned} \mathbf{x}_k &= \mathbf{f}(\mathbf{x}_{k-1}, \mathbf{u}_{k-1}) + \mathbf{w}_{k-1} \\ \mathbf{y}_k &= \mathbf{h}(\mathbf{x}_k) + \mathbf{v}_k \end{aligned} \quad (2.26)$$

where $\mathbf{x}_k = \begin{bmatrix} \boldsymbol{\omega}_k \\ \mathbf{q}_k \end{bmatrix}$ is the process state (plant); \mathbf{u}_k is the control input (e.g. \mathbf{T}_C).

$$\mathbf{f}(\mathbf{x}_{k-1}, \mathbf{u}_{k-1}) = \begin{bmatrix} \boldsymbol{\omega}_{k-1} \\ \mathbf{q}_{k-1} \end{bmatrix} + \Delta t \begin{bmatrix} \mathbf{I}^{-1} [\mathbf{T}_C + \mathbf{T}_D - (\boldsymbol{\omega}_{k-1} \times \mathbf{I} \boldsymbol{\omega}_{k-1})] \\ \frac{1}{2} \boldsymbol{\Omega}(\boldsymbol{\omega}_{k-1}) \mathbf{q}_{k-1} \end{bmatrix} \quad (2.27)$$

and $\mathbf{y}_k = \begin{bmatrix} \mathbf{y}_{G,k} \\ \mathbf{y}_{q,k} \end{bmatrix}$, with $\mathbf{y}_{G,k}$ given in Eq. (2.24) and $\mathbf{y}_{q,k}$ given by Eq. (2.10). Due to the nonlinearity of Eq. (2.27), the system is first linearized to obtain the Jacobian matrices \mathbf{F} and \mathbf{H} ,

$$\begin{aligned} \mathbf{F}_{k-1} &= \left. \frac{\partial \mathbf{f}}{\partial \mathbf{x}} \right|_{\hat{\mathbf{x}}_{k-1}^+, \mathbf{u}_{k-1}}, \\ \mathbf{H}_k &= \left. \frac{\partial \mathbf{h}}{\partial \mathbf{x}} \right|_{\hat{\mathbf{x}}_k^-} = I_{7 \times 7}, \end{aligned} \quad (2.28)$$

where the superscript $-$ and $+$ represent a *priori* and a *posteriori* state estimates and EKF is implemented as a two-step process. In the predictor step,

$$\begin{aligned} \hat{\mathbf{x}}_k^- &= \mathbf{f}(\hat{\mathbf{x}}_{k-1}, \mathbf{u}_{k-1}), \\ \mathbf{P}_k^- &= \mathbf{F}_{k-1} \mathbf{P}_{k-1} \mathbf{F}_{k-1}^T + \mathbf{Q}_{k-1} \end{aligned} \quad (2.29)$$

where \mathbf{P} is the error covariance matrix. In the update step, the Kalman filter gain is calculated first

$$\mathbf{K}_k = \mathbf{P}_k^- \mathbf{H}_k^T (\mathbf{H}_k \mathbf{P}_k^- \mathbf{H}_k^T + \mathbf{R}_k)^{-1}, \quad (2.30)$$

and the state-estimate is updated with the optimal gain:

$$\hat{\mathbf{x}}_k^+ = \hat{\mathbf{x}}_k^- + \mathbf{K}_k \left(\mathbf{y}_k - \mathbf{h}(\hat{\mathbf{x}}_k^-) \right). \quad (2.31)$$

The error covariance matrix is updated for use at the predictor step

$$\mathbf{P}_k^+ = \left[I_{7 \times 7} - \mathbf{K}_k \mathbf{H}_k \right] \mathbf{P}_k^- = \left[I_{7 \times 7} - \mathbf{K}_k \right] \mathbf{P}_k^-. \quad (2.32)$$

3.4. Attitude Control

In this section, the thruster model and control implementation are introduced and the change of angular velocity during one set of thruster firings is discussed as well as thruster arrangement. Then the attitude control methods using μ PPTs are discussed. Sidi (2000) discusses pulse-width pulse-frequency modulation (PWPF) method; however, the fixed pulse duration and the restricted pulse frequency f_p of μ PPT has limited the use of PWPF. Two control methods are developed: paired firing method, and separation control algorithm and thruster allocation methods.

3.4.1. Thruster Model and Control Implementation

The thruster model is derived in the BRF shown in Figure 1-1a. The origin is placed in the center of mass of the CubeSat and the Z-axis is along the long axis and is positive towards the thruster side. Thrusters numbered 1 to 4 are on the top layer and 5 to 8 are on the second layer as shown in Figure 3-3. The positioning of the thrusters provides redundancy in attitude control. The μ PPT operates as shown in Figure 2-5.

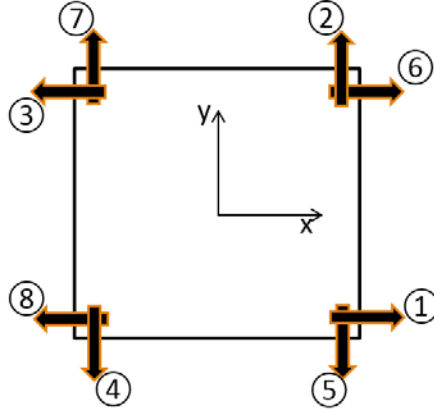


Figure 3-3: Top view of thruster arrangement (1, 2, 3, 4 are on the top layer).

A discrete-time dynamic model of Eq. (2.1) is required due to the pulsed operation of the thrusters,

$$\mathbf{I} \frac{\Delta \boldsymbol{\omega}}{\Delta t} = [\mathbf{T}_C + \mathbf{T}_D - (\boldsymbol{\omega} \times \mathbf{I} \boldsymbol{\omega})] . \quad (2.33)$$

The torque \mathbf{T}_i , produced by a single firing of one μ PPT during τ_p is

$$\mathbf{T}_i = F (\mathbf{r}_{eff,i} \times \mathbf{n}_i) = \frac{I_{bit}}{\tau_p} (\mathbf{r}_{eff,i} \times \mathbf{n}_i) . \quad (2.34)$$

and then the control torque \mathbf{T}_C from a set of active thrusters during τ_p is

$$\mathbf{T}_C = \sum_{i \in \mathbf{I}(t)} \left[\frac{I_{bit}}{\tau_p} (\mathbf{r}_{eff,i} \times \mathbf{n}_i) \right] , \quad (2.35)$$

where $\mathbf{I}(t) = \{1, 2, \dots\}$ is the set of active thrusters which is determined later in thruster allocation and the effective position vector of the thrusters from the center of mass is defined as

$$\mathbf{r}_{eff,i} = \mathbf{r}_i - \mathbf{r}_{com} , \quad (2.36)$$

where \mathbf{r}_i is the position vector of the thruster relative to the CubeSat's geometrical center, and \mathbf{r}_{com} is the vector from the geometric center to the center of mass. Assuming that the control torque is applied during $\Delta t = \tau_p$ upon substitution of Eq. (2.34) into Eq. (2.33) it becomes

$$\mathbf{I}\Delta\boldsymbol{\omega} = \sum_{i \in \mathbf{I}(t)} \left[I_{bit} (\mathbf{r}_{eff,i} \times \mathbf{n}_i) \right] + \mathbf{T}_D \tau_p - (\boldsymbol{\omega} \times \mathbf{I} \boldsymbol{\omega}) \tau_p. \quad (2.37)$$

Scaling of the above equation can be obtained using typical values for $I_x = 0.03 \text{ kg} \cdot \text{m}^2$, $I_{bit} = 40 \times 10^{-6} \text{ N} \cdot \text{m}$, $\|\mathbf{r}_{eff,i}\| = 0.15 \text{ m}$, $\|\mathbf{T}_D\| = 6 \times 10^{-6} \text{ N} \cdot \text{m}$, $\tau_p \sim 10^{-6} \text{ s}$, $\boldsymbol{\omega} < 0.15 \text{ rad/s}$. The last two terms in the RHS of Eq. (2.37) can be neglected and Eq. (3.37) becomes:

$$\Delta\boldsymbol{\omega} = \mathbf{I}^{-1} \sum_{i \in \mathbf{I}(t)} \left[I_{bit} (\mathbf{r}_{eff,i} \times \mathbf{n}_i) \right]. \quad (2.38)$$

Notice that the pulse frequency f_p , does not affect the change of angular velocity for each firing, but given a time span, frequency will affect the total number of firings, which influences the total change of angular velocity.

I also account for the shot-to-shot variation, so the output I_{bit} is equal to the designed $\overline{I_{bit}}$ plus a random error with a Gaussian distribution and standard deviation of one percent

$$I_{bit} = \overline{I_{bit}} + \delta(t). \quad (2.39)$$

A fixed error for the thrust vector \mathbf{n}_i was introduced to account for thrust misalignment with respect to the BRF. The thruster vector \mathbf{n}_i is rotated by 0.5 degs in each of the two off-axis directions to simulate a constant error introduced during structure integration.

3.4.2. Paired Firing Technique

To effectively control the attitude, given the specific arrangement of thrusters that was discussed in the thruster model section shown in Figure 3-3, “paired firings” is utilized, which means that each control command fire two thrusters simultaneously (given that both thrusters are available). The idea is assuming the center of mass is very close to the geometric center, by pairing two thruster, one axis of reaction can be produced and the off-axis reactions are roughly cancelled.

Table 3-1: Thruster pairs for paired firing method

Control over	Positive Direction	Negative Direction
<i>X</i> -axis	Thruster 2 and 7	Thruster 4 and 5
<i>Y</i> -axis	Thruster 3 and 8	Thruster 1 and 6
<i>Z</i> -axis	Thruster 5 and 7	Thruster 1 and 3
	Thruster 6 and 8	Thruster 2 and 4

The main assumption for this method is that the center of mass of the satellite lies around the geometric center with no more than 3cm away. From the table above, at most four thrusters can be fired simultaneously in any situations. Per the restriction from the design of the pulsed thruster, maximum five thrusters can operate at the same time; as a result, this is a valid firing strategy.

3.4.2.1. Stabilization & Spinning

In order to stabilize the satellite, the angular velocity is needed to be regulated. Using paired firing, each axis is considered separately and at most two axes are regulated which are considered in descending order of priority, based on the magnitude of angular velocity. The

approach is to control the axis with the largest angular velocity first. Figure 3-4 depicts the flow chart summarizing the control strategy with ω_{th} denoting the angular velocity at which the CubeSat is considered as stabilized. The value of ω_{th} cannot be too small due to the dynamics of the pulsed thruster and must be larger than the uncertainty of the gyroscope as well as the impulsive change in the angular velocity due to each paired firings. Note that “No action” in the flow chart represents no control is performed.

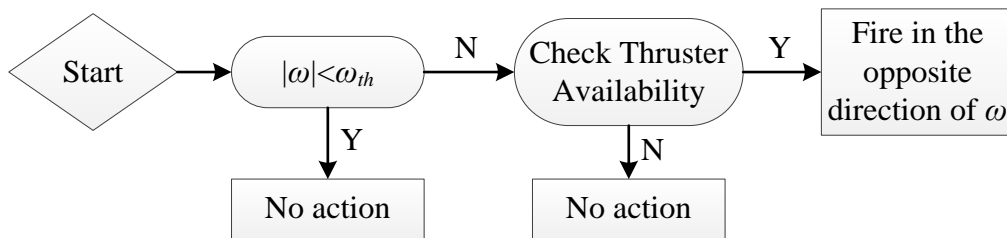


Figure 3-4: Control strategy for stabilization using paired firing method

3.4.2.2. Pointing (Slew) Maneuvers

Similar to the control strategy for stabilization, for pointing control each axes is also considered separately. Yaw, pitch and roll angles of the BRF can be obtained in terms of the MRF and each angle is being regulated to zero in order to achieve the pointing requirement. Pointing requires the satellite to orient itself from an arbitrary position to a desired position, which is in principle similar to a slew maneuver. Therefore, successfully controlling the satellite to a desired attitude also enables the slew maneuvers. The only difference between the two is that during a slew maneuver, a fast time is always preferable where for static pointing; the fuel consumption may be more of a concern. Figure 3-5 shows a flowchart of the pointing control strategy for one axis.

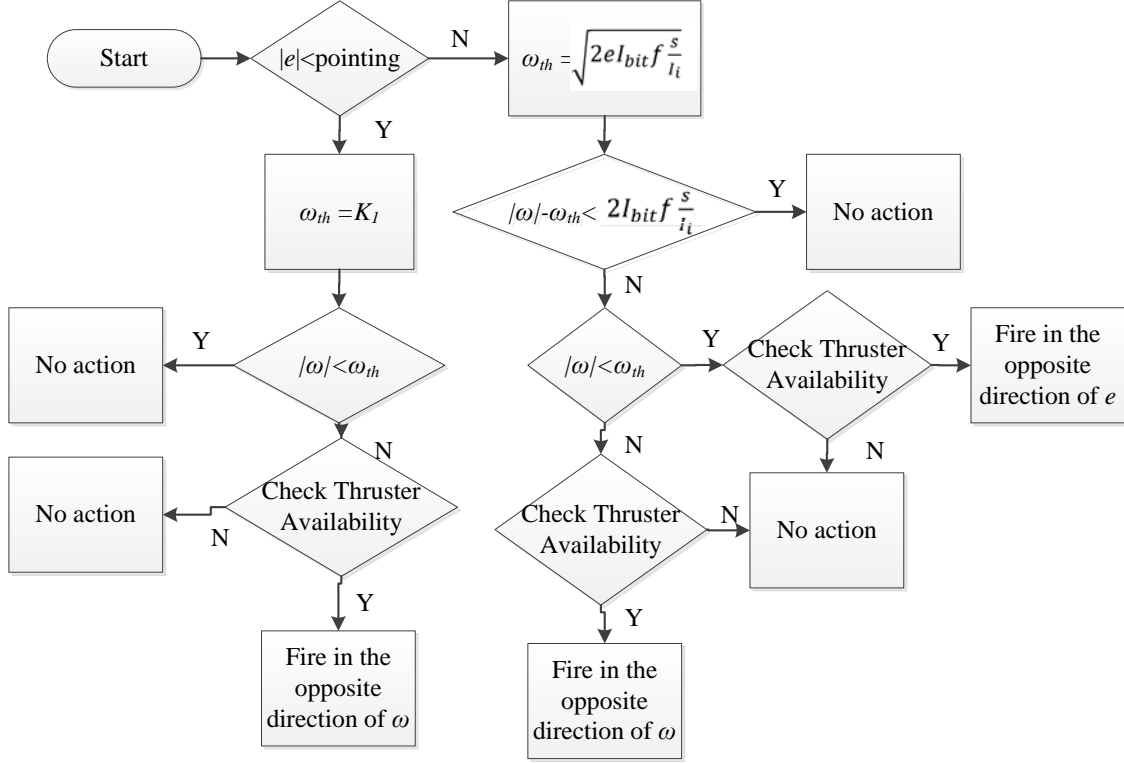


Figure 3-5: Control strategy for pointing using paired firing method

3.4.2.3. Optimal Angular Velocity Threshold for Pointing

The optimal angular velocity threshold for this study is defined as the maximum angular velocity that can be achieved in the process of correcting the attitude (within the capability of the thrusters) and minimum overshoot. The threshold depends on the error angles (i.e. yaw, pitch, and roll angles). The optimal threshold takes the shortest time to achieve a certain attitude. One axis case is first considered which the result is applied to all three axes. The change of angular velocity by each firing is determined by

$$\Delta\omega = \frac{I_{bit} \cdot \|\mathbf{r}_{eff}\|}{I} \quad (2.40)$$

Note that for one axis I is a scalar, for 3 axes $\bar{\mathbf{I}}^{-1}$ is a 3x3 matrix. Similar to the relation between displacement and acceleration, the equation regarding the angle, angular velocity and angular acceleration is

$$\zeta = \frac{1}{2}\ddot{\zeta}t^2 + \dot{\zeta}_0t + \zeta_0, \quad (2.41)$$

where, $\ddot{\zeta} = \Delta\omega \cdot f$ is the angular acceleration for the μ PPT, and $\dot{\zeta}_0$ is the initial angular velocity, which is assumed to be 0 for this analysis.

I introduce $e = \zeta - \zeta_0$ as the angle travelled due to the angular acceleration, is given by

$$e = \frac{1}{2}\Delta\omega ft^2 \quad (2.42)$$

The time for the controller to move the angle by e radians is

$$\Delta t = \sqrt{\frac{360e}{\Delta\omega f \pi}} \quad (2.43)$$

In addition, ideally the angular velocity should be 0 when the error angle is 0. As a result, given a specific angle error, the max angular velocity allowed is

$$\omega_{th} = t_{op}\Delta\omega \cdot f = \sqrt{2eI_{bit}f \frac{\|\mathbf{r}_{eff}\|}{I_i}} \quad (2.44)$$

Assuming the initial angular velocity is zero, Figure 3-6 shows that, for a 5 degree error angle, the shortest recovery time can be achieved if the μ PPT is saturated (i.e. operating at maximum thrust). In order to validate our analysis, four control policies are compared which have different angular velocity thresholds vs error angle curves. In Figure 3-7, policy #1 denotes the optimal threshold (Blue curve), policy #2 (Green curve) and policy#3 (Red curve) denote the cases in

which the system undershoot and policy #4 (Light blue) denotes the case of an overshoot. Note that the minimum angular velocity deadband cannot be smaller than the sensor error; otherwise, the error will result in unnecessary firings thus wasting propellant.

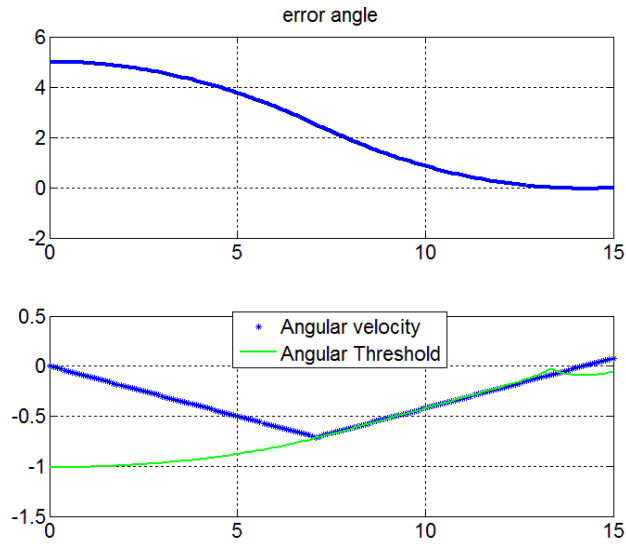


Figure 3-6: Depiction of optimal angular velocity threshold.

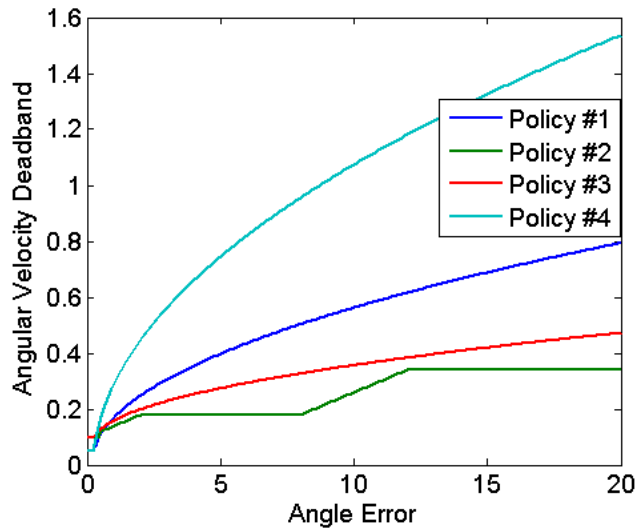


Figure 3-7: Four policies featuring different angular velocity threshold vs error angle.

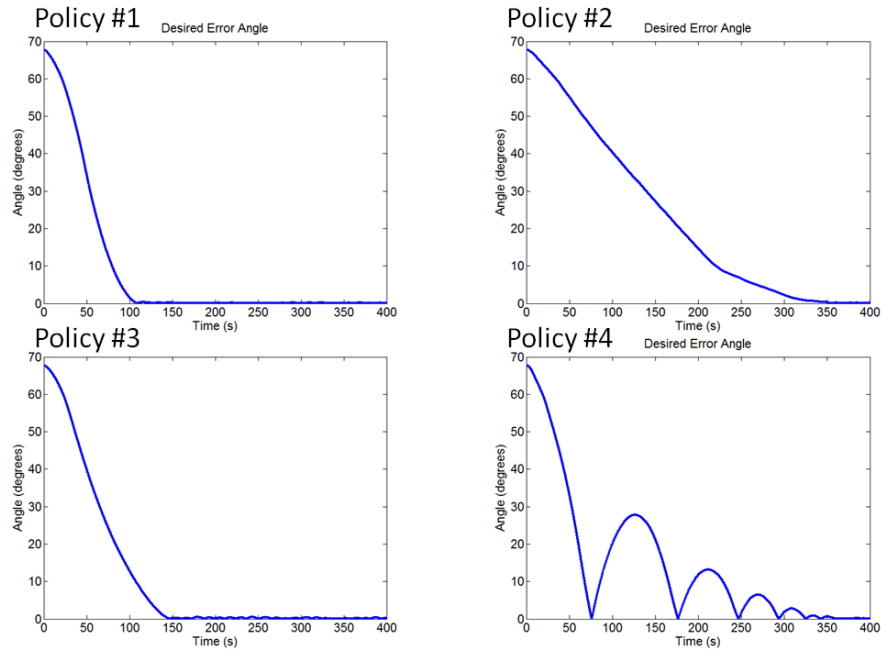


Figure 3-8: Comparison of pointing accuracy with different policies.

Figure 3-8 shows that when the thresholds are low (e.g. policy #2 and #3), it takes longer for the CubeSat to point in the correct direction. When the thresholds are large (policy #4), it overshoots and the result is that the pointing takes much longer time to converge. Obviously, the policy with the optimal threshold gives the best result. A smaller threshold leads to slower slew and longer time to converge whereas a large threshold leads to unwanted overshoot and waste of propellant. Figure 3-9 shows that for policy #1 the maximum angular velocity achieved is at approximately 1 degree/s, whereas for policy #2 and #3 the maximum is smaller and it takes longer time to correct the pointing error. For policy #4, the maximum angular velocity is 1.5 deg/s and results show that it causes the system to overshoot. These results validate that the optimal threshold is optimal.

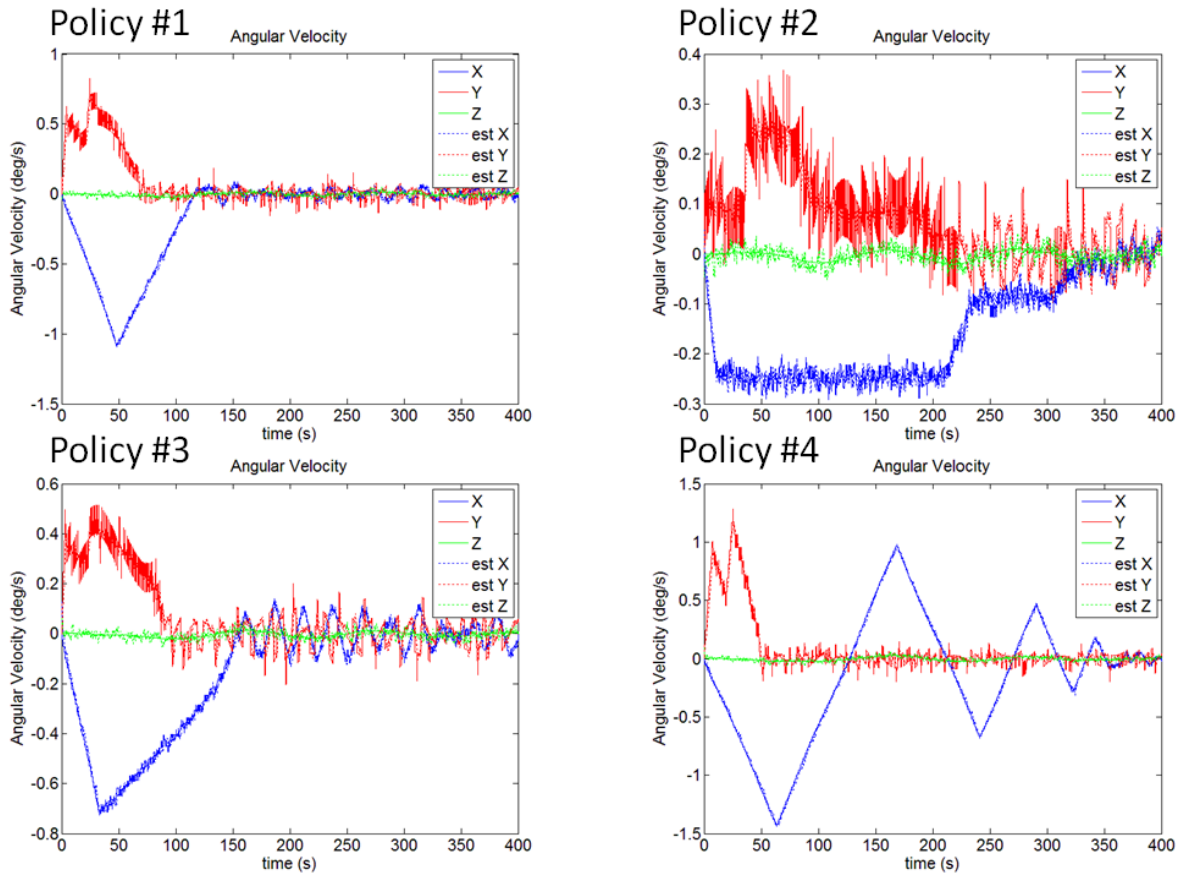


Figure 3-9: Comparison of angular velocity profile for different policies for pointing.

The angular velocity threshold determines the allowed maximum angular velocity, and the angle deadband is introduced which determines the allowable excursion from the desired angle. The performance of policy #1, #2, and #3 are listed in Table 3-2 with angle deadbands of 0.1 degree and 0.25 degree. The time needed to achieve 0.5 degree accuracy provides us an estimate of how fast the CubeSat will achieve the desired pointing; and the percentage under 0.5 degrees measures the quality of the policy. The average number of pulses indicates the propellant consumption required by each policy. The results indicate that policy #1 requires faster times, higher percentage. Obviously, with a 0.1 degree angle deadband, the thruster is fired much more

than with 0.25 degree. As a result, to keep the pointing under certain angle and to save fuel, it is desirable to have the largest angle deadband possible.

Table 3-2: Performance comparison of control policies for pointing

Policy	Angle deadband (degree)	Time to achieve 0.5 degree (sec)	2-norm of error angle (rads)	Percentage under 0.5°	Average No. of pulses
#1	0.1	105.4	2.219	94.73%	1175
#1	0.25	105.6	2.215	94.68%	545
#2	0.1	334.16	2.628	83.30%	1070
#2	0.25	334.88	2.626	83.26%	526
#3	0.1	143.93	2.280	91.72%	1059
#3	0.25	143.89	2.281	92.44%	537

In summary, policy #1 was the best option to achieve correct attitude with the shortest time and the least amount of propellant consumption.

3.4.2.4. Spinning with Pulsed Thruster

The control for spinning is similar to that for stabilization except that in stabilization, the desired angular velocity is 0 for all axes, whereas for spinning, the desired angular velocity is nonzero. It has shown that the spinning along the short axes are naturally unstable, so for the simulation of spinning, the maximum rotational speed of each axis is investigated so that the thruster can control the attitude properly. The analysis is shown in the simulation results in Chapter 4.

3.4.2.5. Pointing and Spinning with Pulsed Thruster

Control strategy for spinning and pointing follows the strategies for pointing and stabilization. The desired pointing is first achieved and then the angular velocity around the spinning axis is increasing incrementally (if the angle is off the desired value, correction to the angle is made first following by spinning up).

3.4.3. Control using Separate Controller Algorithm and Thruster allocation

As shown in Figure 3-10, the process commences with the attitude determination and estimation to produce the estimates $\hat{\omega}(t)$ and $\hat{\mathbf{q}}(t)$. Then the estimated states $\hat{\omega}(t)$ and $\hat{\mathbf{q}}(t)$ from EKF are used in proportional and derivative control algorithm in place of $\omega(t)$ and $\mathbf{q}(t)$ in order to calculate the desired torque \mathbf{T}_{des} . Note that the actuator system cannot realize the desired torque \mathbf{T}_{des} using μ PPT due to the fixed impulse bit; as a consequence, a thruster allocation method is utilized to determine the best thruster firing combination $\mathbf{z} \in \mathbf{R}^n$ such that the angle between \mathbf{T}_{des} (the designed control input using Eq. (2.1) and (2.2)) and control output \mathbf{T}_C (the actual input to Eq. (2.1) and (2.2) which is the output of the μ PPT) is minimal. Finally, the control torque output \mathbf{T}_C is computed and is used to actuate the control system given by Eq. (2.1) and (2.2). One advantage of using a two-step process for attitude control, i.e. a separate control algorithm and thruster allocation, is to increase the robustness of attitude control in the event of thruster failure.

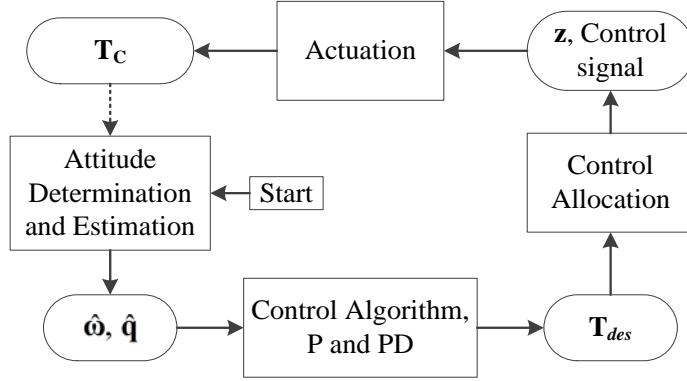


Figure 3-10: Flow chart for attitude control.

3.4.3.1. Stabilization

During the stabilization phase, attitude determination is not required and only the estimate of the angular rate $\hat{\omega}$ is needed, and the desired torque is

$$\mathbf{T}_{des} = -\mathbf{K}(\hat{\omega} - \omega_{des}) \quad (2.45)$$

where \mathbf{K} is a user-defined proportional gain matrix and ω_{des} is the desired angular velocity. If the actuator had no dynamics, then this \mathbf{T}_{des} is implemented in Eq. (2.1) as \mathbf{T}_C . However, as mentioned above, thruster allocation method finds the best thruster firing combination that minimizes the angle between the desired torque \mathbf{T}_{des} and the control torque \mathbf{T}_C delivered by the active μ PPTs.

3.4.3.2. Target Pointing (Slewing) and Spinning

A general PD controller using Euler error angles, ϕ , is used as the control algorithm

$$\mathbf{T}_{des} = -\mathbf{K}_p \boldsymbol{\varphi} - \mathbf{K}_d (\hat{\boldsymbol{\omega}} - \boldsymbol{\omega}_{des}) \quad (2.46)$$

In the case of sun pointing, two of the Euler angles can be obtained directly from the sun sensors. In general, they are given by

$$\boldsymbol{\varphi} = \begin{bmatrix} \tan^{-1}(2\tilde{q}_1\tilde{q}_4 + 2\tilde{q}_2\tilde{q}_3, 1 - 2\tilde{q}_1^2 - 2\tilde{q}_2^2) \\ \sin^{-1}(2\tilde{q}_4\tilde{q}_2 - 2\tilde{q}_3\tilde{q}_1) \\ \tan^{-1}(2\tilde{q}_3\tilde{q}_4 + 2\tilde{q}_1\tilde{q}_2, 1 - 2\tilde{q}_2^2 - 2\tilde{q}_3^2) \end{bmatrix} \quad (2.47)$$

Where the function, \tan^{-1} with two arguments is the four quadrant inverse tangent which differs from the regular inverse tangent by expanding the output range from $[-\pi/2, \pi/2]$ to $[-\pi, \pi]$.

The error quaternion $\tilde{\mathbf{q}}$ is defined in Wie (2008) as

$$\tilde{\mathbf{q}} = \begin{bmatrix} \tilde{q}_1 \\ \tilde{q}_2 \\ \tilde{q}_3 \\ \tilde{q}_4 \end{bmatrix} = \begin{bmatrix} q_{des,4} & q_{des,3} & -q_{des,2} & -q_{des,1} \\ -q_{des,3} & q_{des,4} & q_{des,1} & -q_{des,2} \\ q_{des,2} & -q_{des,1} & q_{des,4} & -q_{des,3} \\ q_{des,1} & q_{des,2} & q_{des,3} & q_{des,4} \end{bmatrix} \begin{bmatrix} q_1 \\ q_2 \\ q_3 \\ q_4 \end{bmatrix} \quad (2.48)$$

where \mathbf{q}_{des} can be found in the reference model. In Eq. (2.46), \mathbf{K}_p and \mathbf{K}_d are proportional and derivative gain matrices which are determined by the moment of inertia of the spacecraft:

$$\begin{aligned} \mathbf{K}_p &= 2\omega_n^2 \mathbf{I} \\ \mathbf{K}_d &= 2\zeta\omega_n \mathbf{I} \end{aligned} \quad (2.49)$$

where ω_n and ζ are the natural frequency and damping ratio, and which require tuning in order to achieve acceptable attitude control performance. Due to the limited control authority of a

pulsed thruster, the damping ratio does not work in the same way as with a traditional controller. In this case, the direction of the desired torque provided by the PD control scheme is more important than the magnitude of the torque. Different gain matrices may be chosen based on different specifications and arrangement of the μ PPT. The performance of the controller also depends on the accuracy of the sensor (i.e. the statistics of the noise $\mathbf{v}(t)$ in Eq. (2.25) and the magnitude of the environmental disturbances $\mathbf{T}_D(t)$ in Eq. (2.1).

3.4.3.3. Optimal Controller Allocation

The angle between the torque output, \mathbf{T}_C and the desired torque, \mathbf{T}_{des} (i.e. the cost function) must be minimized in order to obtain the best approximation of \mathbf{T}_{des} . This is solved with a nonlinear binary optimization:

$$\min_{\mathbf{z}} \left\| \cos^{-1} \left(\frac{\mathbf{Bz} \cdot \mathbf{T}_{des}}{\|\mathbf{Bz}\| \|\mathbf{T}_{des}\|} \right) \right\|, \quad (2.50)$$

subject to: $\mathbf{z} \in \{0, 1\}^n$ and $\sum_{i=1}^n z_i \leq 5$

where \mathbf{z} is a $n \times 1$ vector indicating the status of all thrusters where each entry has value of either 0(off) or 1(on), and $\mathbf{B} \in \mathbb{R}^{m \times n}$ is the control effectiveness matrix (i.e. $\mathbf{B}_i = (\vec{r}_{eff,i} \times \vec{n}_i)$), where $n = 8$ is the length of \mathbf{z} , and $m = 3$ is the length of \mathbf{T}_{des} (Oppenheimer & Doman, 2006). Notice that \mathbf{z} is the control signal that determines which thruster to fire, and \mathbf{Bz} is the actuator output (also is \mathbf{T}_C). The second condition in Eq. (2.50) is the constraint from the thruster electronics. Preliminary design of the thruster module has constrained the power distribution to an upper limit of 5 thrusters at one time, which means that at any instance, at most 5 thrusters can be fired,

i.e. the cardinality of the set $\mathbf{I}(t)$ is at most 5 at any instance. Solution to this optimization provides the best thruster firing combinations to accommodate the direction of desired torque.

If the cost function is twice continuously differentiable, the solution can be obtained by first convexifying the problem and then solving a sequence of subproblems, whose solutions form a trajectory that leads to the final solution (Murray & Ng, 2010). However, this is not the case because the cost function cannot be simplified; the only way to solve this optimization problem is by method of exhaustion. Fortunately, there are only eight binary variables which require 255 repeated calculations and it is practical to solve it onboard in real-time. The cosine is an even function, with $\cos(0) = 1$. Therefore, the cost function can be reduced to a simpler form:

$$\min_{\mathbf{z}} \left\{ -\frac{\mathbf{Bz} \cdot \mathbf{T}_{des}}{\|\mathbf{Bz}\| \|\mathbf{T}_{des}\|} \right\} \quad (2.51)$$

subject to: $\mathbf{z} \in \{0, 1\}^n$ and $\sum_{i=1}^n z_i \leq 5$

This reduces the computational cost. Although the improvement is on the level of tenth of milliseconds, but it could be significant in cases that \mathbf{z} has a large dimension. When the desired attitude is achieved, a deadzone modification was implemented in order to avoid unnecessary thruster firings:

$$\mathbf{T}_{des,i} = \begin{cases} \mathbf{T}_{des,i} & , \quad |\mathbf{T}_{des,i}| > \mathbf{T}_{crit} \\ 0 & , \quad |\mathbf{T}_{des,i}| \leq \mathbf{T}_{crit} \end{cases} \quad (2.52)$$

where T_{crit} is the critical torque threshold which is determined based on the moment of inertia \mathbf{I} , effectiveness matrix \mathbf{B} , and impulse bit I_{bit} . When the desired torque is below the critical torque level, no thruster is active, which means if $\mathbf{T}_{des} = 0$, \mathbf{z} is a 8×1 vector of zeros and $\mathbf{I}(t)$ is the null set.

This control algorithm is processed no more frequent than the pulse frequency of the μ PPT. So for a μ PPT of $f_p = 1$ Hz, the algorithm is evaluated at most once every second. The advantage of using this method is also that, during the event of thruster failure, simply changing the \mathbf{B} matrix in the optimization will suffice.

Chapter 4.

Simulations of Mission Scenarios and Results

To validate the control algorithms that were developed in section 3.4, the spacecraft dynamic is simulated and the control algorithms are implemented in MATLAB[®]. In section 4.1, the input parameters used in simulation to obtain the results is introduced (such as CubeSat parameters and thruster properties). Then in section 4.2, 4.3, and 4.4, the simulation results are presented and compared for both control methods developed in section 3.4 for the three scenarios: stabilization, pointing, and pointing and spinning. The performance is compared with the estimates from thruster sizing in section 2.3.2. The power and fuel consumption during each scenario is also presented and discussed. In section 4.5, simulation results are presented to show how the thruster failure affects the performance of both control methods, and why having a thruster allocation method increases the redundancy in the controller.

4.1. Input Parameters

For simulation purposes, MATLAB[®] is utilized to implement the attitude control for the CubeSat shown in Figure 1-1b. The center of mass of the CubeSat in the BRF is located at $[0.5 \ 1.5 \ -1]$ cm relative to the geometric center. The inertia matrix (non-diagonal) for the CubeSat shown in Figure 1-1b is estimated as:

$$I = \begin{bmatrix} 0.03 & 0.0005 & 0.0005 \\ 0.0005 & 0.03 & 0.0005 \\ 0.0005 & 0.0005 & 0.006 \end{bmatrix} \text{ kg} \cdot \text{m}^2$$

I assume that the μ PPT has $I_{bit} = 40 \mu\text{N} \cdot \text{s}$ with a random error of normal one percent and a pulse frequency $f_p = 1 \text{ Hz}$. The thrust vector has a fixed error of 1% to simulate error introduced in the thruster-structure integration. Since the orbit propagation was not considered in this study, the orbital parameters of the CubeSat are not evaluated. In order to study the feasibility of a μ PPT in providing the desired attitude control, a periodic disturbances torques based on the maximum disturbances encountered in the orbit is introduced and the disturbances are applied to all three axes.

Typical sensor errors are introduced in the simulation. Sun sensors have error of 0.5 degrees (3σ); gyroscope has error of 0.05 deg/s and magnetometer has error of 250 nT. The gains for thruster allocation methods are: $\zeta = 3.7$ and $\omega_n = 0.1$.

4.2. Stabilization Results

After being deployed from the launch vehicle, a CubeSat usually has random rotations and the first phase of attitude control is to stabilize the CubeSat. The initial body rotation rate is assumed to be 5 deg/s in each axis. At the end of stabilization phase, the CubeSat should have a minimum angular rotation as some onboard buses and hardware are powered on.

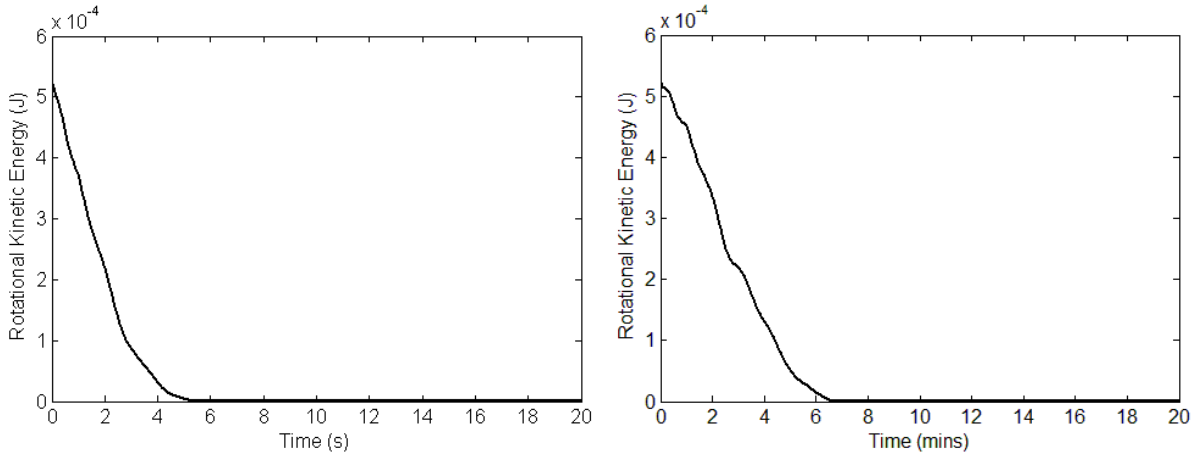


Figure 4-1: Rotational kinetic energy of a CubeSat undergoing stabilization with paired firing (left) and thruster allocation (right).

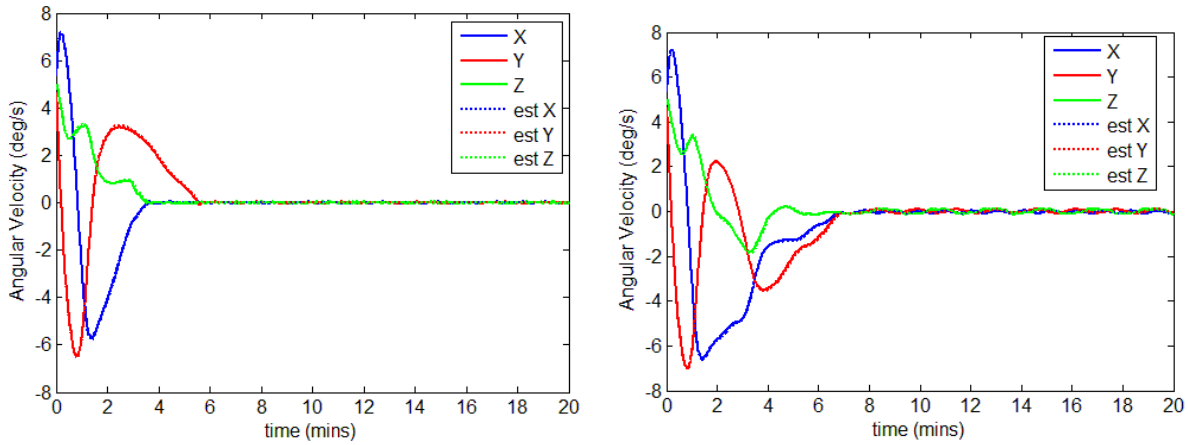


Figure 4-2: Angular velocity of a 3U CubeSat undergoing stabilization with paired firing (left) and thruster allocation (right).

The thruster has fixed impulse bit, so the result is different from the usual controller where an exponential decay is expected. From the data presented in Figure 2-6 and Figure 2-7, in section 2.3, a set of six thrusters, operating with an impulse bit and pulse frequency of $40 \mu\text{N}\cdot\text{s}$ and 1 Hz respectively, is found to be capable of completing maneuvers with an angular momentum rate of under $5 \mu\text{N}\cdot\text{s/s}$. So for a stabilization of $\Delta\omega=5 \text{ deg/s}$, the time estimate is a little less than 10 minutes, which is consistent with the result presented here. The stabilization time is expected to be less than an estimate based solely on the rate, due to the addition of two thrusters. In this

regards, both methods achieves the stabilization within our estimated time. But paired firing has a slight edge in achieving stabilization compared with the thruster allocation method. The reason for this advantage will be clear when the power consumption by both methods is analyzed later.

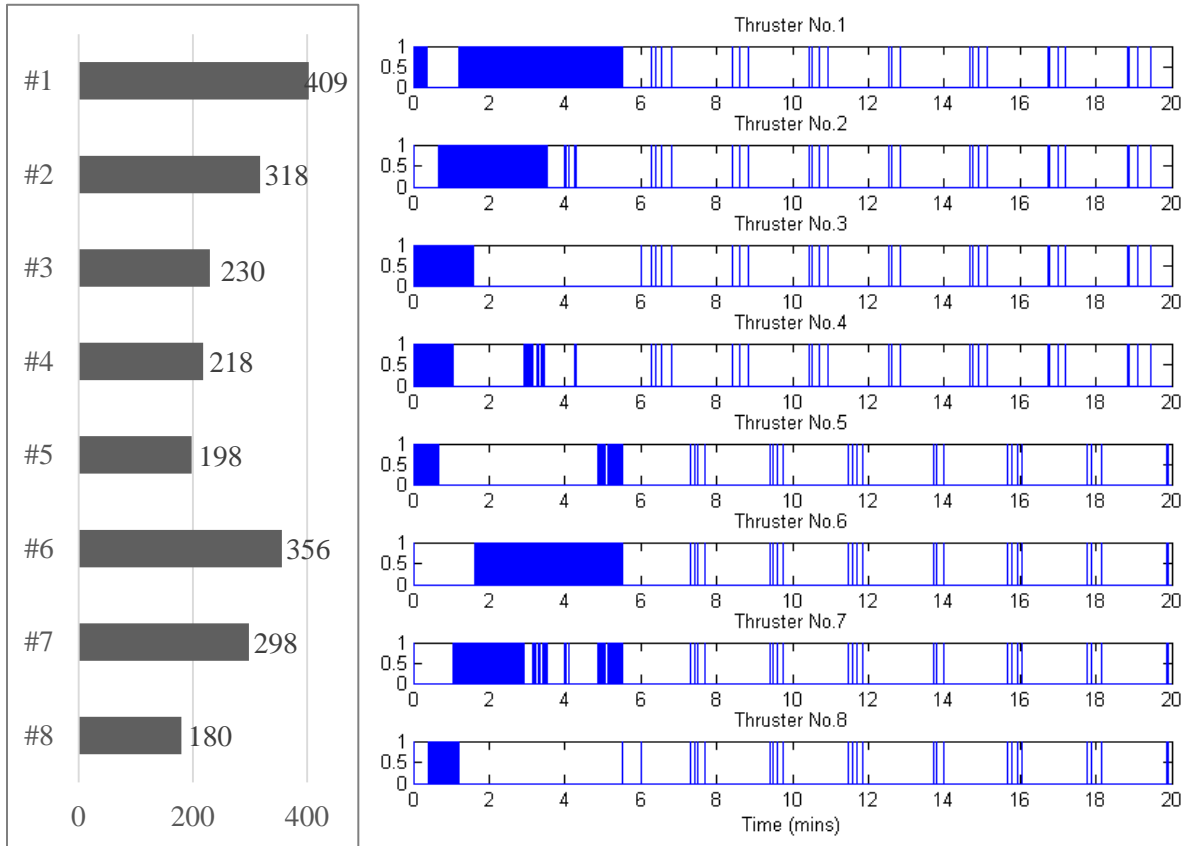


Figure 4-3: Firing sequence of μ PPTs on a 3U CubeSat during stabilization and compensation of periodic disturbance using paired firing; (Left) the total number of firings from each thruster; (Right) the time of occurrence for each firing indicted by a line. The areas filled with lines indicate that the specific thruster is on full operation.

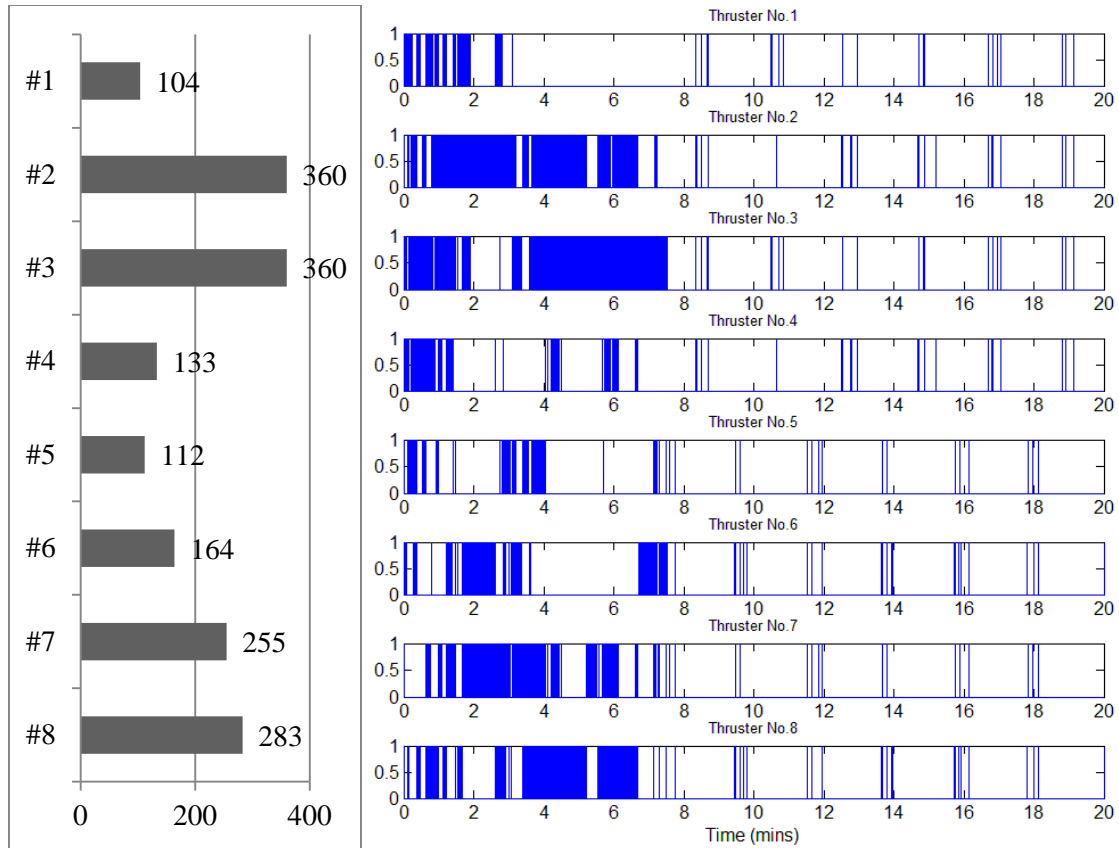


Figure 4-4: Firing sequence of μ PPTs on a 3U CubeSat during stabilization and compensation of periodic disturbance using thruster allocation; (Left) the total number of firings from each thruster; (Right) the time of occurrence for each firing indicted by a line.

For μ PPTs, the amount of fuel consumption is proportionally related to the number of firings. Figure 4-3 also represents the amount of fuel consumed during the maneuver. From Figure 4-3 and Figure 4-4, paired firing method uses more fuel than thruster allocation method (during 20-min window, total number of firing is 2200 for paired firing method and 1771 for thruster allocation method). Thruster allocation utilizes the best possible firing combination for a proportional controller, as a result, the effective impulse bit by each firing combination is maximized, but to achieve this effectiveness, the performance (i.e. time for stabilization) is not ideal. However, paired firing method uses a pair of thrusters, due to the cancellation of the torque along the off-axis direction, the effective impulse bit is reduced. Looking closely at Figure 4-1

for paired firing, the rotational kinetic energy decreases almost linearly for the first 2.5 minute, but the slope of the curve decreases afterward, especially after 4 minutes. In Figure 4-2 for pair firings, after 4 minutes, both X and Z axes are stabilized which leaves only the Y -axis. It started by four thrusters firing simultaneously to regulate either two of the three axes; however, only two thrusters have the capability to regulate in one direction along the Y -axis, meaning that the decrease of the rotational kinetic energy will slow down due to fewer firing thrusters.

The same pattern can be found when comparing power consumption by both methods during stabilization. A typical shot energy of 1.5 J is used to calculate the power consumption of a μ PPT module. In Figure 4-5, using paired firings, the average power consumption for stabilization is fixed at 6 W for the first 3 minutes, and then gradually decreases to less than 1W, whereas the average power consumption for stabilization is approximately 6 W, and after 8 minutes when the CubeSat is stabilized, the average power consumption is less than 1W for disturbance torque compensation using thruster allocation. With double deployed solar panels shown in Figure 1-1b, the total power generation during sunlight is rated at 20 W, as a result, the power consumption is well within the constraint of a CubeSat power budget.

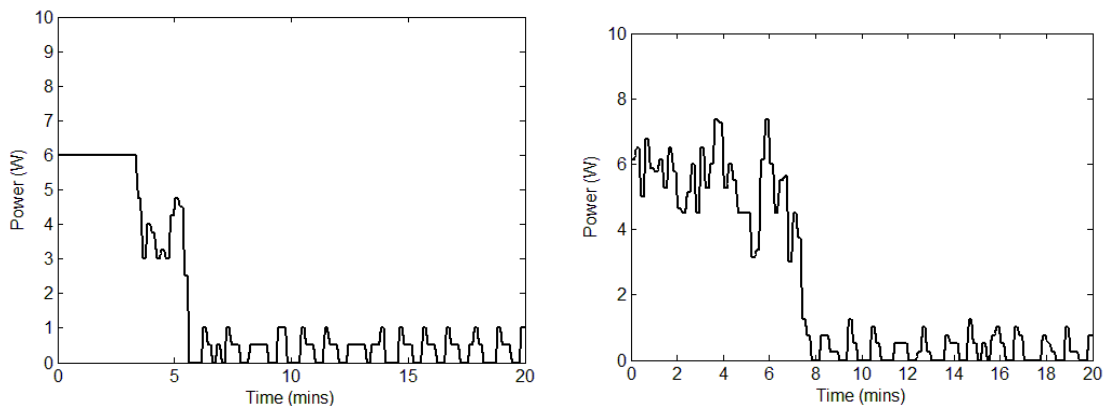


Figure 4-5: Power consumption of μ PPTs on a 3U CubeSat during stabilization and compensation of periodic disturbance torques with paired firing (left) and thruster allocation (right).

After the CubeSat is stabilized, there are scattered firings as shown in both Figure 4-3 and Figure 4-4. The scattered firings after 8 min. compensate for the rotation due to disturbance torques. Comparing this with the result due to a constant disturbance torque in Figure 4-6, the thrusters can stabilize the CubeSat in both situations and the time for initial stabilization is similar; however, it requires more firings to compensate for the constant disturbance torques which act on the spacecraft continuously.

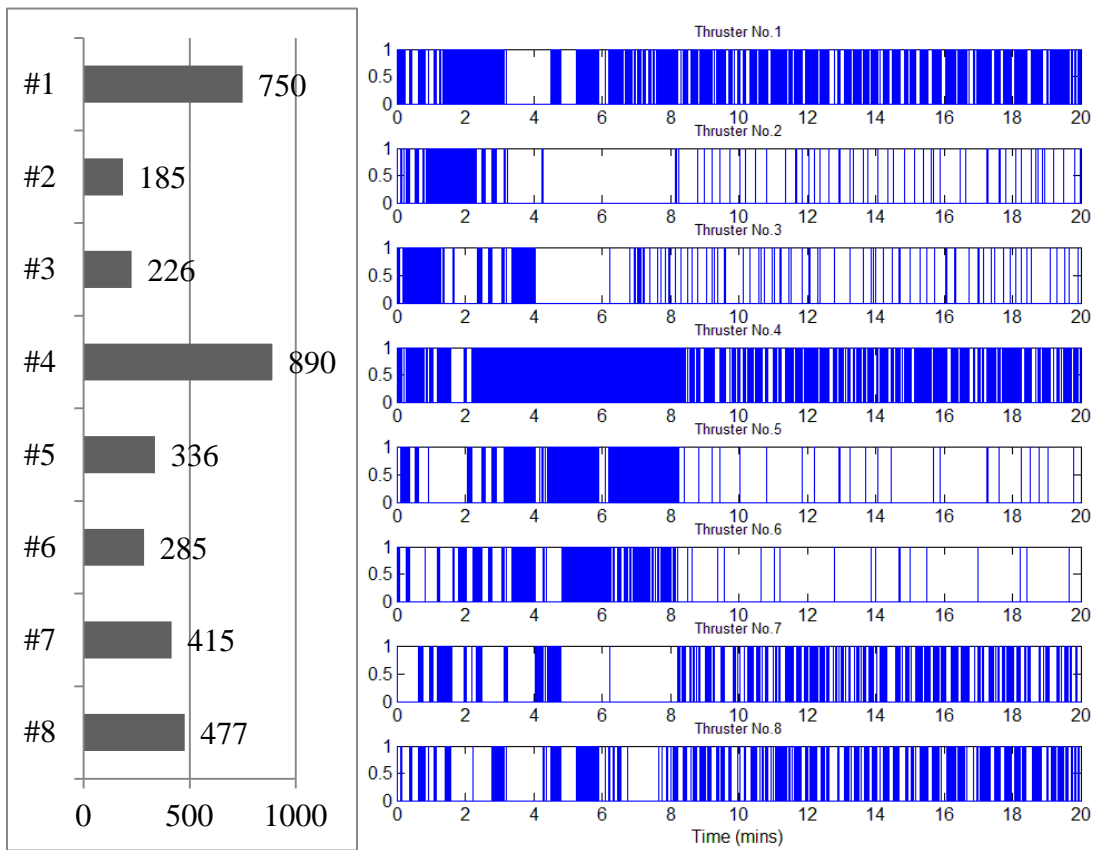


Figure 4-6: Firing sequence of μ PPTs on a 3U CubeSat during stabilization and compensation of the maximum constant disturbance. (Left) The total number of firings from each thruster; (Right) the time of occurrence for each firing indicted by a line.

As noted earlier, to compensate for a constant disturbance requires a set of six thrusters with $40\mu\text{N}\cdot\text{s}$ with 1 Hz frequency. With the specific arrangement of thrusters in this study, $n=2$ in

Eq. (1.16) and as a result none of the thrusters is overloaded. The μ PPT is adequate to stabilize the CubeSat even during the worst case of disturbance.

4.3. Pointing Results

A CubeSat mission considered in this scenario involves Sun observation or target tracking. In this simulation, the initial error angle about the Sun is 68 degrees and it is required that the CubeSat be controlled to correctly point toward the Sun within 0.5 degrees. This leads us to the pointing requirement where the CubeSat needs to be oriented correctly to have the desired field-of-view over a certain target. The Allowable time span for the maneuver is set to 20 minutes.

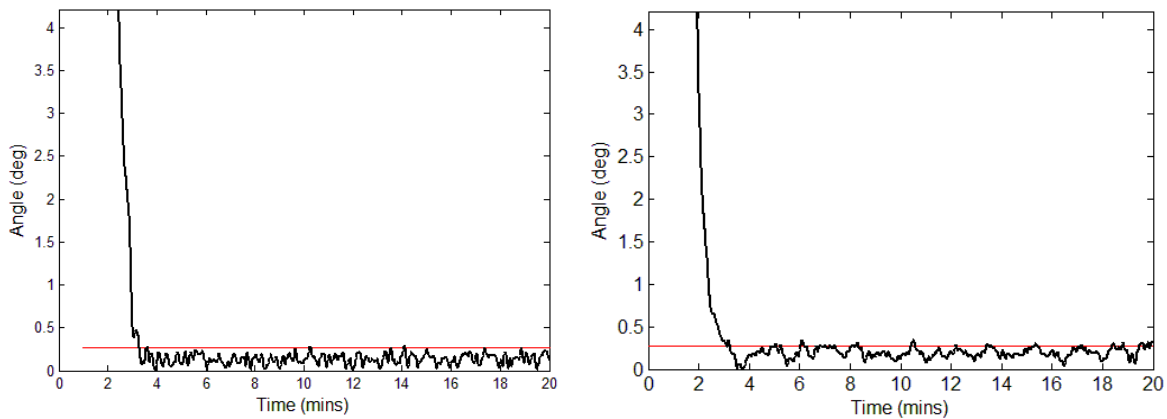


Figure 4-7: Pointing angle error of a 3U CubeSat using μ PPTs with paired firing (left) and thruster allocation (right).

The pointing accuracy is limited by the sensor accuracy. A fine Sun sensor has accuracy within 0.1 degrees however a coarse Sun sensor more commonly encountered will have an accuracy of 0.1 to 1 degree. Figure 4-7 shows the pointing error during the 20-min simulation. The red line shows the radius of the Sun in the view from CubeSat. Both methods achieve within 5 degree accuracy in approximately 2 minutes, and thruster allocation method takes longer to

achieve fine pointing (i.e. below the red line). Comparing the pointing accuracy by both methods in long term, they have very similar performance; the pointing accuracy can be achieved under 0.5 degrees. In Figure 4-8, the angular velocities for the first 2 minutes depicts the fastest slew maneuver which can be achieved by μ PPTs. The angular velocity reaches maximum and starts to decrease immediately, implying the idle (or coasting) period is 0%.

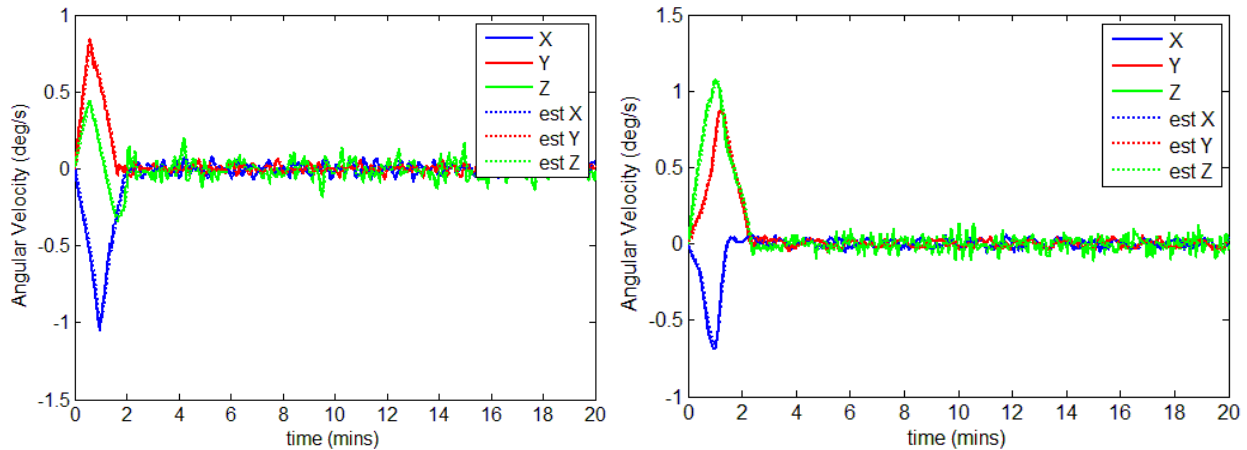


Figure 4-8: Angular velocity of a 3U CubeSat undergoing pointing using μ PPTs with paired firing (left) and thruster allocation (right).

Fuel consumption during pointing maneuver is then investigated for both control methods. Figure 4-10 and Figure 4-11 represents the firings for paired firing method and thruster allocation method respectively. From the time occurrence of firings, in both methods, thrusters are constantly firing to compensate for the disturbance torques, but it appears that paired firing achieves the same level of pointing accuracy with less fuel consumption. The average number of firing by each thruster for pair firing method is a 275, whereas that of thruster allocation method is 475. Paired firing has a clear advantage in fuel consumption and it uses 40% less than thruster allocation method

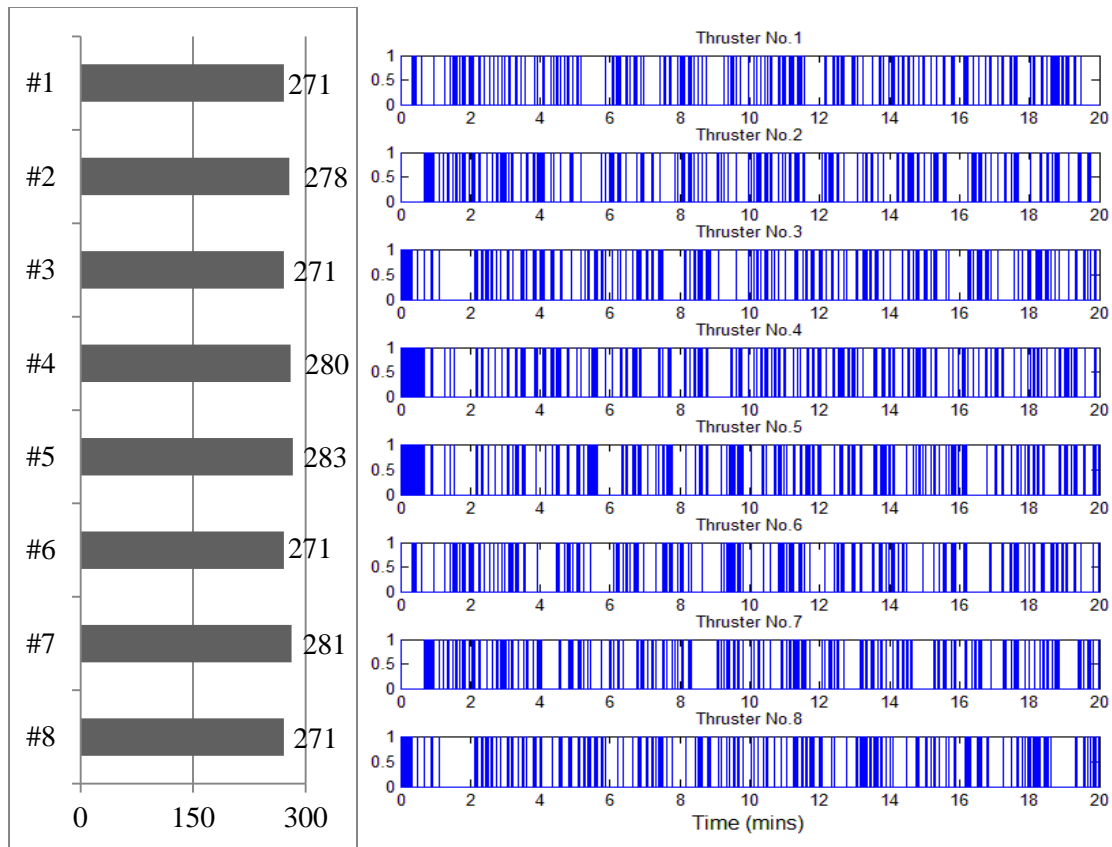


Figure 4-9: Firing sequence of μ PPTs on a 3U CubeSat during pointing with paired firing allocation. (Left) The total number of firings from each thruster; (Right) the time of occurrence for each firing indicted by a line.

In Figure 4-10, the average number of pulses per thruster is 472, with minimum 419 and maximum 517. Assuming that the CubeSat is always in the view of the Sun for a desired mission time of one year, then the average number of pulses is approximately 12 million/thruster and the maximum number of pulses is 13 million/thruster. Similarly to stabilization, Figure 4-11 shows the power consumption of the μ PPT module during pointing maneuvers. It is expected that at most 5 thrusters are fired at the same time and under normal operation, 2 to 4 thrusters are fired constantly to correct the pointing and compensate for the disturbance torques so the power consumption is between 3 to 6 W.

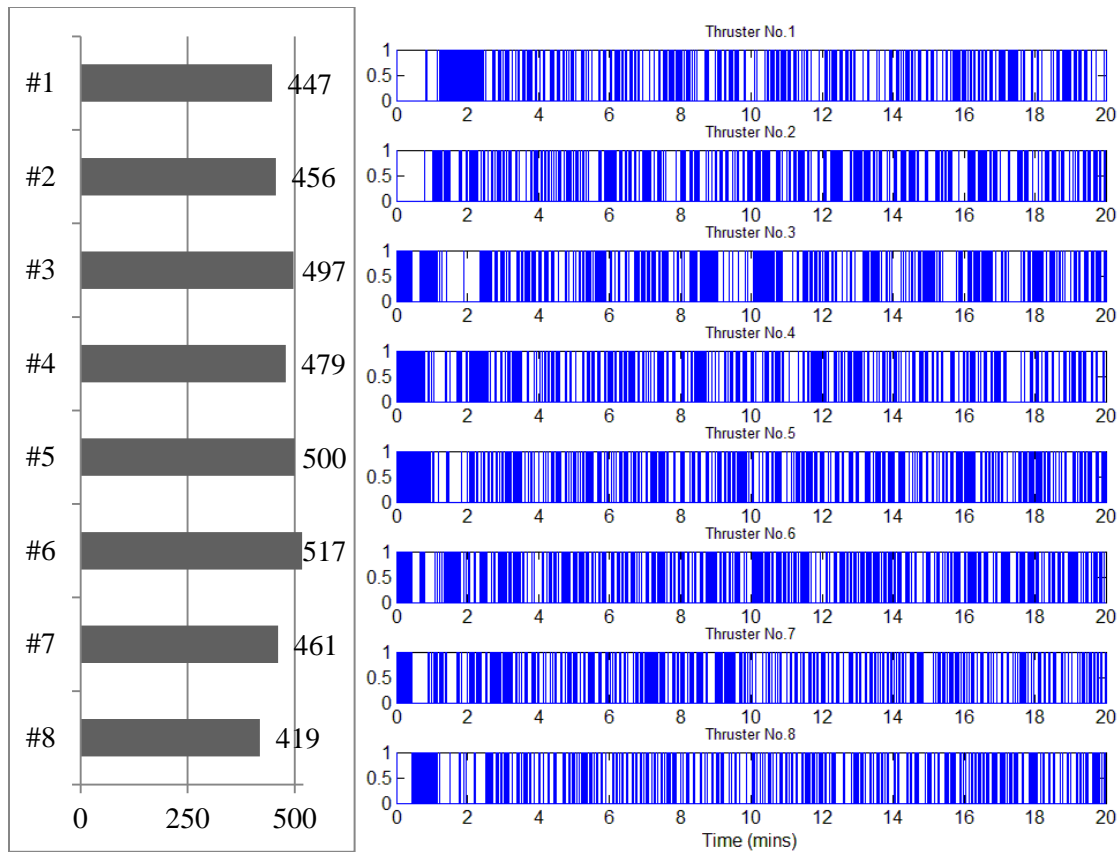


Figure 4-10: Firing sequence of μ PPTs on a 3U CubeSat during pointing with thruster allocation. (Left) The total number of firings from each thruster; (Right) the time of occurrence for each firing indicted by a line.

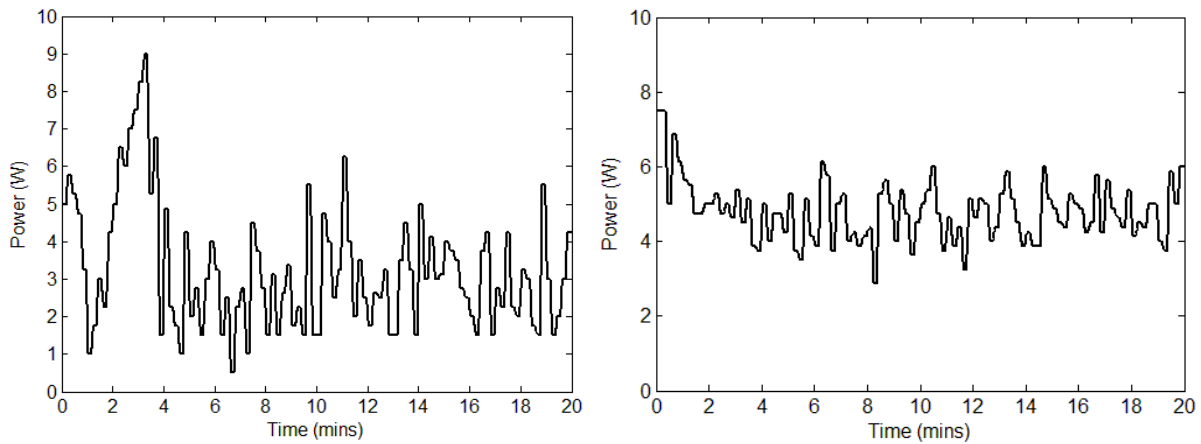


Figure 4-11: Power consumption of μ PPTs on a 3U CubeSat during pointing with paired firing (left) and thruster allocation (right).

4.4. Pointing and Spinning Result

In this simulation, the control strategy for spinning and pointing is evaluated. The strategy will orient the CubeSat towards the Sun within 0.5 degree and then start to spin it to 3 deg/s around the pointing axis. Figure 4-12 shows that the CubeSat first initiate the pointing maneuver to obtain the desired attitude. Then it starts to spin around the pointing axis. As the CubeSat is constantly adjusting the attitude for pointing, thrusters may fire for pointing correction thus no or fewer thrusters will be available for spinning. Figure 4-13 shows the angular velocity of a CubeSat undergoing spinning and pointing maneuvers using both control methods.

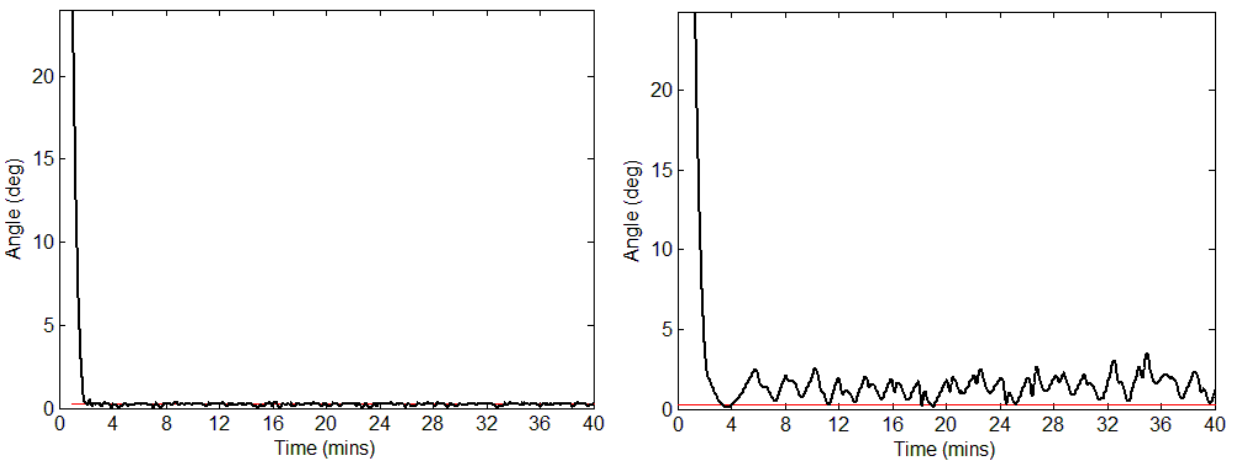


Figure 4-12: Pointing angle error of a 3U CubeSat undergoing spinning and pointing maneuvers using μ PPTs with paired firing (left) and thruster allocation (right).

It is obvious that paired firing achieves a much more stable spinning and pointing than thruster allocation method. There is a drastic difference between the performances for pointing and spinning maneuver using paired firing and thruster allocation. The reason can be seen by considering the pointing result in section 4.3 where thruster allocation utilizes more number of firings for the similar performance of pointing maneuver. Every thruster is more occupied using

thruster allocation method than using paired firing for pointing maneuver, and in turn, less control output can be distributed towards spinning up the CubeSat.

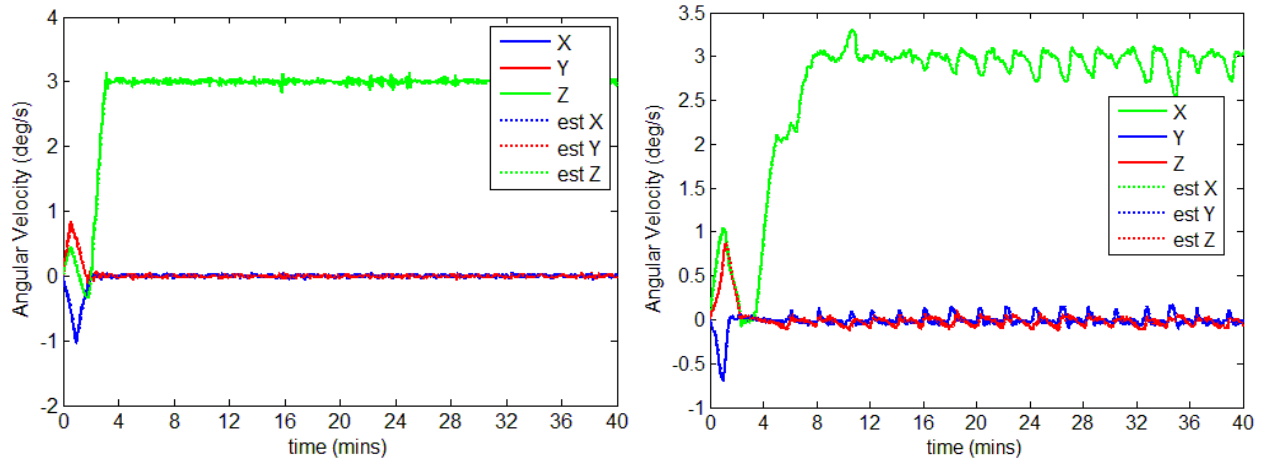


Figure 4-13: Angular velocity of a 3U CubeSat undergoing pointing and spinning to 3 deg/s using μ PPTs with paired firing (left) and thruster allocation (right).

In Figure 4-15, the time for the CubeSat to spin up to 3 deg/s in one axis, is approximately 2 min. Because the pointing axis is a major axis where moment of inertia is the largest among all three axes, the rotation is relatively stable.

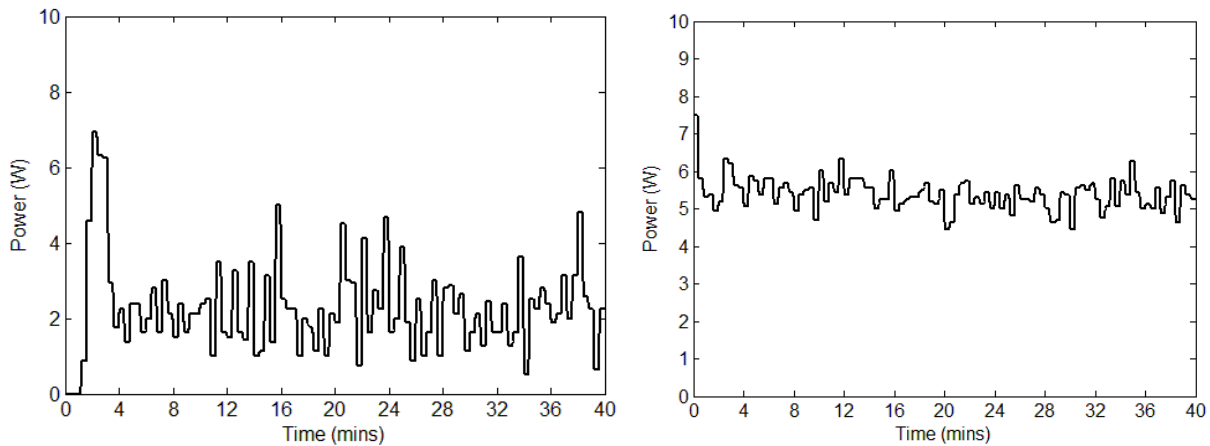


Figure 4-14: Power consumption of μ PPTs on a 3U CubeSat during pointing with paired firing (left) and thruster allocation (right).

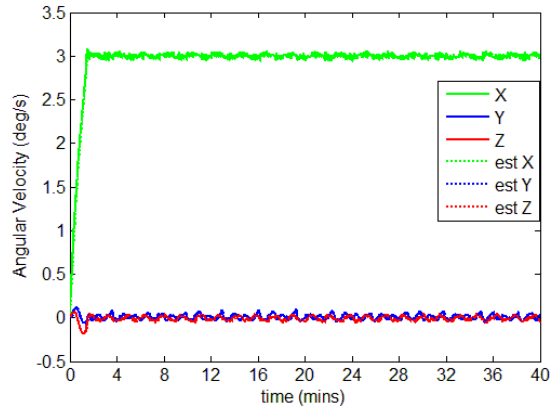


Figure 4-15: Angular velocity of a 3U CubeSat undergoing spinning to 3 deg/s without pointing using μ PPTs with thruster allocation.

4.5. Pointing Performance with Thruster Failure

This section compares simulation results during pointing maneuvers with the thruster-allocation method and paired-firing method. Thruster #3 is set to be inoperative and detection of the failure is assumed. Paired firing will use the same technique with the optimal angular velocity threshold being halved due to the loss of half control authority, but when the pair of thrusters which includes thruster #3 is commanded to fire, only the operational thruster will fire. With the separate control algorithm and thruster-allocation method, as described in Section 3.4.3, the control effectiveness matrix needs to be modified to accommodate the situation and the gain in the control algorithm will be affected, as was the case when decreasing the threshold for the paired firing technique.

Figure 4-16 shows the pointing accuracy and demonstrates that both methods are able to orient the CubeSat properly with the thruster allocation method being more robust. The time required to achieve pointing and stabilization with thruster failure is slightly longer than that without failure as a comparison with Figure 4-7. A comparison of the angular velocity of the

CubeSat in Figure 4-17, shows that the paired-firing method does not eliminate the constant angular velocity around the pointing axis because it cannot properly distribute the torque. In contrast, the thruster allocation method shows that the impact of the thruster failure is minimal.

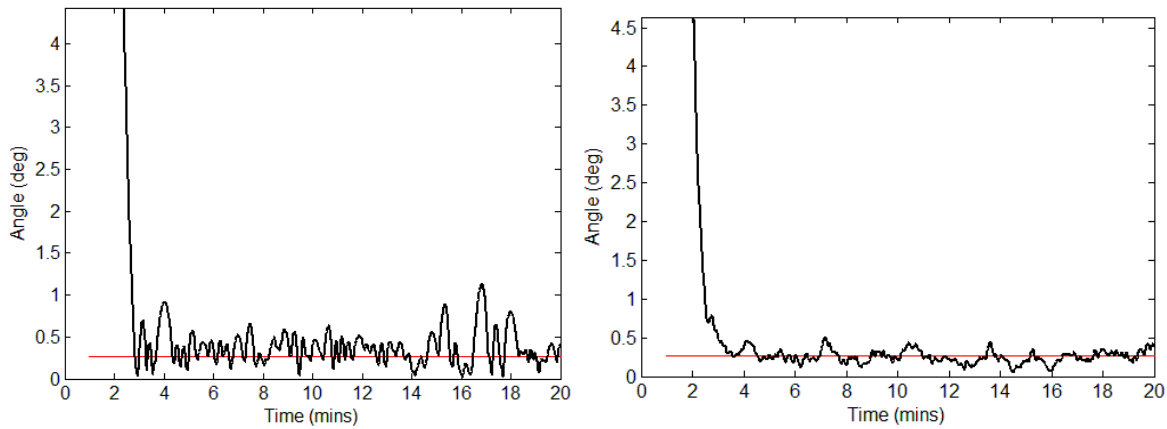


Figure 4-16: Pointing angle error of a 3U CubeSat using μ PPTs with paired firing (left) and thruster allocation (right) under thruster failure.

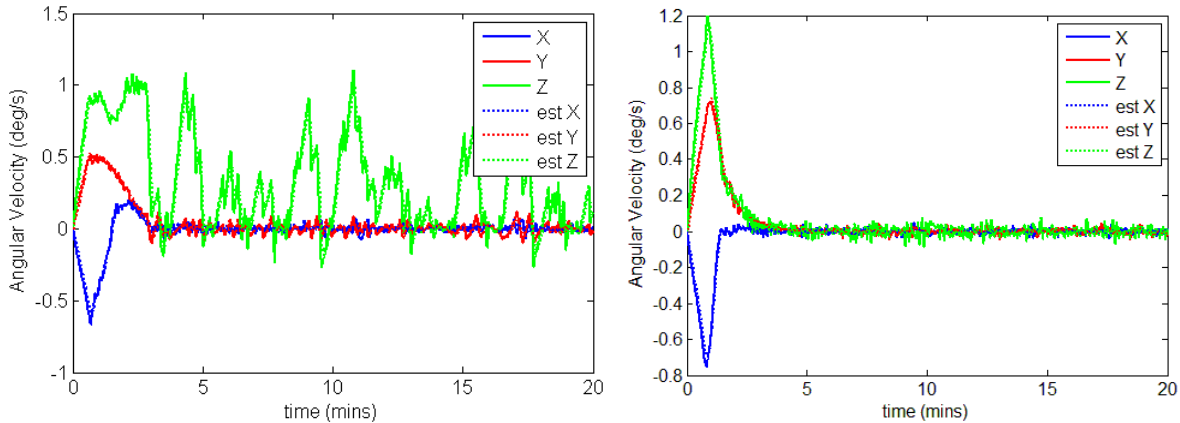


Figure 4-17: Angular velocity of a 3U CubeSat using μ PPTs with paired firing (left) and thruster allocation (right) under thruster failure.

Now comparing the power consumption for both methods in Figure 4-18, despite having the advantage of consuming less fuel and power during normal operation, paired firing method consumes significantly more power and in turn more fuel for a pointing maneuver with a failed thruster.

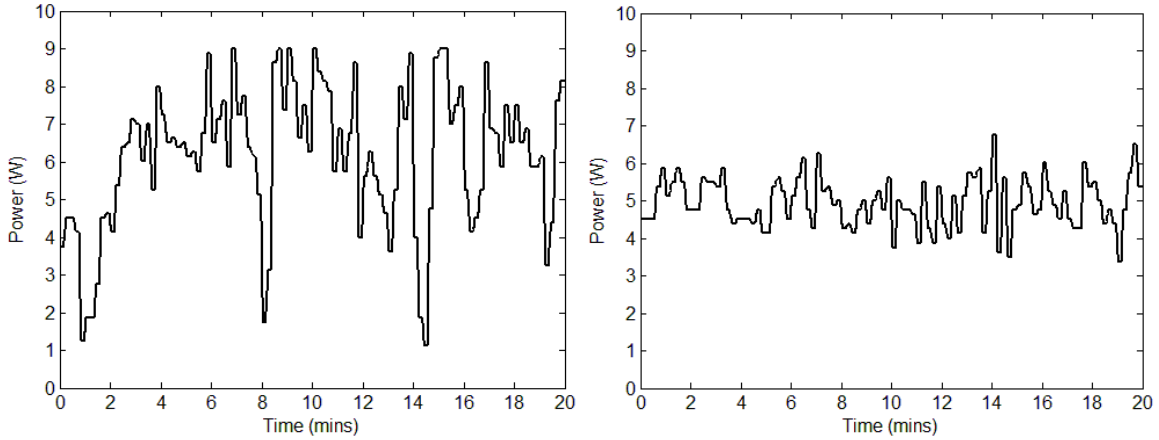


Figure 4-18: Power consumption of μ PPTs with paired firing (left) and thruster allocation (right) under thruster failure.

Without loss of control authority, thruster #3 and #6 are set as inoperative. The simulation results are shown in Figure 4-19 and Figure 4-20. Both control methods achieve pointing with the thruster-allocation method exhibiting better performance. As before, the paired-firing method fails to stabilize the rotation along the Z axis.

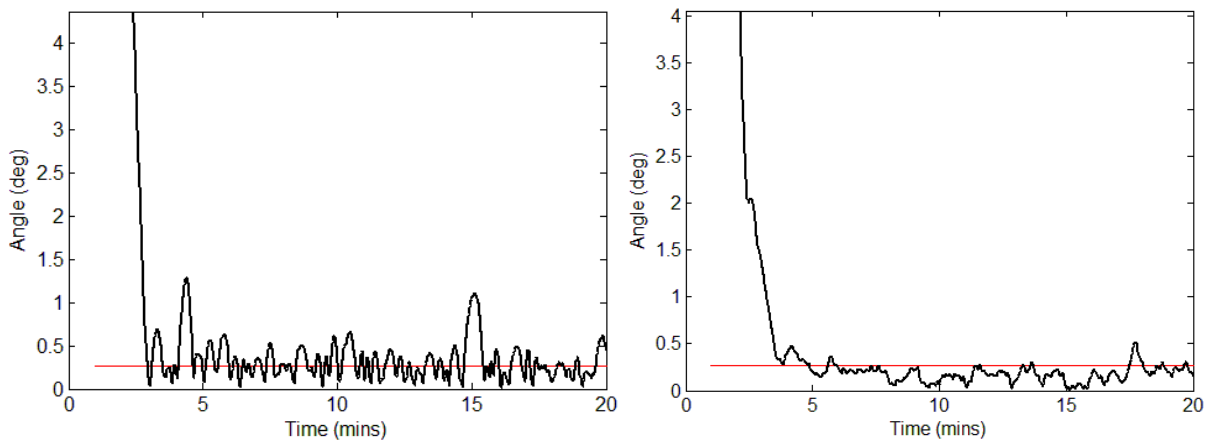


Figure 4-19: Pointing angle error of a 3U CubeSat using μ PPTs with paired firing (left) and thruster allocation (right) under two thruster failure.

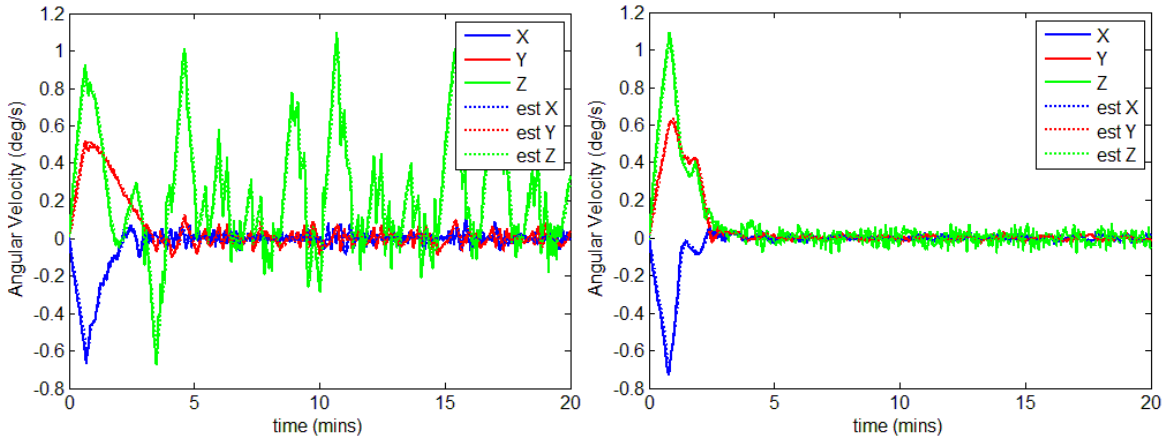


Figure 4-20: Angular velocity of a 3U CubeSat using μ PPTs with thruster allocation (right) under two thruster failure.

Finally thrusters #3, #6, and #7 are assumed to be inoperative and simulation results for the pointing maneuver are shown in Figure 4-21 and Figure 4-22. The paired-firing method is not able to control the attitude properly and can no longer stabilize the CubeSat. The thruster-allocation method can stabilize the CubeSat and maintain the pointing to within an error of 3 degrees.

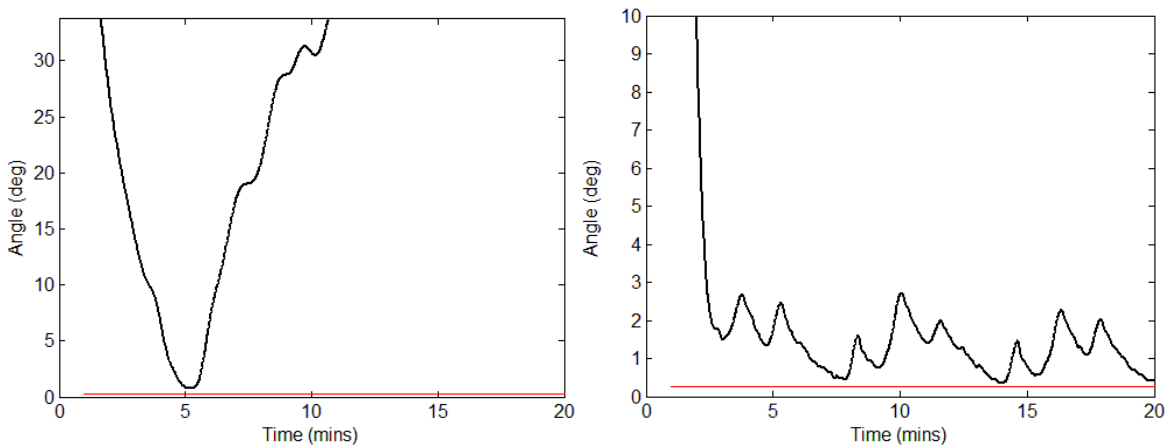


Figure 4-21: Pointing angle error of a 3U CubeSat using μ PPTs with paired firing (left) and thruster allocation (right) under three thruster failure.

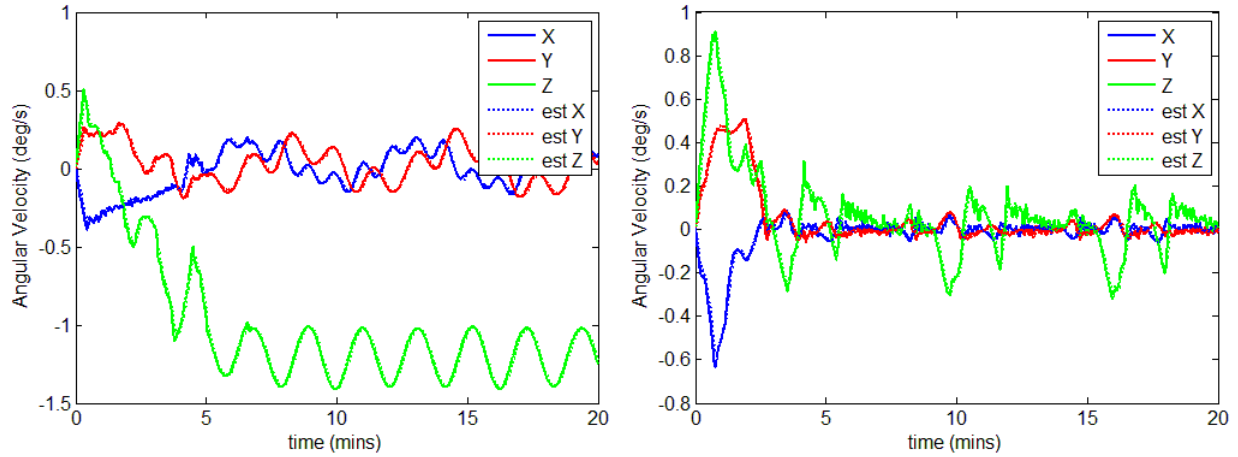


Figure 4-22: Angular velocity of a 3U CubeSat using μ PPTs with paired firing (left) and thruster allocation (right) under three thruster failure.

The results show that the thruster-allocation method has an advantage over the paired-firing especially in cases of thruster failure. The thruster-allocation method can properly distribute the control with the best possible firing combination. Another advantage of thruster allocation method is that it works for arbitrary geometries based on different thruster arrangements. The only parameters to be tuned are the values of proportional and derivative gains, whereas paired firing method only works for the geometry proposed earlier.

Chapter 5.

Summary and Recommendations

This thesis work presents a feasibility study of using μ PPTs for attitude control of 3U CubeSat. The thesis also presents the development of attitude determination, estimation, and attitude control methods.

5.1. Summary

In Chapter 1, a literature review is provided on propulsion options for CubeSat applications along with overall objectives and approaches in this thesis. In Chapter 2, the CubeSat conceptual design is introduced which includes the μ PPT module consisting of 8 thrusters occupying 1U of the CubeSat. The hardware and sensors of the CubeSat are COTS. Sizing of the μ PPT and the propulsion module is based on the magnitude of disturbance torques which can be experienced by the 3U CubeSat in LEO. In Chapter 3, the dynamical model for a rigid body spacecraft is discussed, the actuator model and control implementation for the μ PPT, and useful reference frames. The static attitude determination is obtained using Davenport's q-method. Models for magnetometer and sun sensor, as well as reference models for the Sun's position and the Earth's magnetic field are introduced. The attitude estimation is based on an extended Kalman filter and two control methods. The paired-firing method is developed based on the geometry of the thruster arrangement, whereas a separate control algorithm and thruster-allocation method provide the optimal utilization of the available thrusters. The latter is more robust for attitude

control for arbitrary thruster arrangements or in the event of thruster failure. For the paired firing method, the optimal angular velocity threshold is determined for the shortest time pointing maneuvers.

In Chapter 4, MATLAB simulation results are presented using both control methods for stabilization, pointing, and spinning and pointing. It is shown that both control methods are capable of stabilizing the CubeSat, and they have similar performance in terms of required time. For pointing and pointing with spinning maneuvers, the paired firing method has a clear advantage over the thruster allocation method as paired firing is tailored to the specific thruster arrangement. However in situations of thruster failure, thruster allocation has shown robustness that it is able to accommodate the loss of thrusters.

5.2. Recommendations for Future Work

Future work should involve further development of the propulsion module and the ADC method. Specifically:

- Incorporation of a detailed power budget in the thruster allocation.
- Investigation of additional electric propulsion options.
- Investigation and comparison of alternative control algorithms.
- Development of trade studies to address fuel consumption and time required of maneuvers using various control methods, over longer mission times and under a more expanded set of scenarios.

- Consideration for both attitude and orbital control with the μ PPT module which involves new thruster arrangements and development of different control algorithms and allocation methods as the system may be under-actuated.

References

- Balan, M., Piso, M., Stoica, A. M., Dragasanu, C. G., Trusculescu, M. F., and Dumitru, C. M. 2008. "GOLIAT Space Mission: Earth Observation and Near Earth Environment Monitoring Using Nanosatellites." *59th International Astronautical Congress*. Glasgow, Scotland, UK.
- Bridges, C. P., Kenyon, S., Underwood, C. I., and Sweeting, M. N. 2011. "STRaND: Surrey Training Research and Nanosatellite Demonstrator." *1st IAA Conference on University Satellite Mission and CubeSat Workshop*.
- Clark, C., Guarducci, F., Coletti, M., and Gabriel, S. B. 2011. "An Off-the-shelf Electric Propulsion System for CubeSats." *25th Annual AIAA/USU Conference on Small Satellites*.
- Conklin, J. W., Balakrishnan, K., Buchman, S., Byer, R. L., and et al. 2012. "The Drag-free CubeSat." *AIAA/USU Conference on Small Satellites*. Utah.
- Conversano, R. W., and Wirz, R. W. 2013. "Mission Capability Assessment of CubeSats Using a Miniature Ion Thruster." *Journal of Spacecraft and Rockets* 50: 1035-1046.
- Finlay, C. C., Maus, S., Beggan, C. D., Bondar, T. N., Chambodut, and et al. 2010. "International Geomagnetic Reference Field: the eleventh generation." *Geophysical Journal International* 183 (3): 1216-1230.
- Gatsonis, N. A., Byrne, L., Zwahlen, J., Pencil, E., and Kamhawi, H. 2004. "Current Mode Triple and Quadruple Langmuir Probe Methods with Applications to Flowing Pulsed Plasmas." *IEEE Transactions on Plasma Science* 32 (5): 2118-2129.
- Gatsonis, N. A., Eckman, R., Yin, X., Pencil, E.J., and Myers, R.M. 2001. "Experimental Investigations and Numerical Modeling of Pulsed Plasma Thruster Plumes." *AIAA Journal of Spacecraft and Rockets* 38 (5): 454-464.
- Gatsonis, N. A., Juric, D. and Stechmann, D.P. 2007. "Numerical Analysis of Teflon Ablation in Solid Fuel Pulsed Plasma Thrusters." *43rd AIAA/ASME/SAE/ASEE Joint Propulsion Conference*.
- Gatsonis, N. A., Lu, Ye., Blandino, J. J., Demetriou, M. A., and Paschalidis, N. 2014. "A 3U CubeSat with micro-Pulsed Plasma Thrusters for Attitude Control." *AIAA SPACE Forum*. San Diego.
- Gatsonis, N. A., Lu, Ye., Blandino, J. J., Demetriou, M. A., and Paschalidis, N. 2015 (To be Submitted). "CubeSat Design and Attitude Control with Micro Pulsed Plasma Thrusters." *Journal of Spacecraft and Rockets*.
- Goebel, D. M., Katz, I., 2008. *Fundamentals of Electric Propulsion: Ion and Hall Thrusters*. Hoboken, New Jersey: John Wiley & Sons, Inc.
- Grewal, S. M., and Andrews, P. A. 2008. *Kalman Filtering: Theory and Practice Using Matlab 3rd ed.* New Jersey: Wiley-IEEE Press.
- Hinkley, D., and Hardy, B. 2012. "Picosatellites and Nanosatellites at The Aerospace Corporation." *In-Space Non-Destructive Inspection Technology Workshop*. Johnson Space Center, Houston, TX.

- HM Nautical Almanac Office, US Nautical Almanac Office. 2010. *The Astronomical Almanac 2010: Data for Astronomy, Space Sciences, Geodesy, Surveying, Navigation and Other Applications*. United Kingdom Hydrographic Office.
- JB3-CBS1, Cote, K., Gabriel, J., Patel, B., Ridley, N., Taillefer, Z., Tetreault, S. 2011. *Mechanical, Power, and Propulsion Subsystem Design for a CubeSat*. MQP, Worcester, MA: Worcester Polytechnic Institute.
- JB3-CBS2, Bauer, J., Carter, M., Kelley, K., Mello, E., Neu, S., Orphanos, A., Shaffer, T., Withrow, A. 2012. *Mechanical, Power, and Thermal Subsystem Design for a CubeSat Mission*. MQP, Worcester, MA: Worcester Polytechnic Institute.
- JB3-CBS3, Hanley, J. M., Joseph, B. J., Miller, M. O., Monte, S. J., Trudeau, J. R., and Weinrick, R. L., Advisor: Blandino, J. 2013. *Thermal, Telecommunication and Power Systems for a CubeSat*. MQP, Worcester, MA: Worcester Polytechnic Institute.
- Jong, S., Aalbers, G. T., and Bouwmeester, J. 2008. "Improved Command and Data Handling System for the Delfi-n3Xt nanosatellite." *59th IAC (International Astronautical Congress)*. Glasgow, Scotland, UK.
- Kronhaus, I., Schilling, K., Jayakumar, S. and Kramer, A. 2013. "Design of the UWE-4 Picosatellite Orbit Control System using Vacuum-Arc-Thrusters." *International Electric Propulsion Conference*. Washington, D.C.,
- Laperriere, D., Gatsonis, N. A., and Demetriou, M. A. 2005. "Electromechanical Modeling of Applied Field Micro Pulsed Plasma Thrusters." *41st AIAA/ASME/SAE/ASEE Joint Propulsion Conference & Exhibit*.
- Logan, R., and Greenland, S. 2011. "UKube-1: A Multi-Payload Technology Demonstration Platform." *8th Annual CubeSat Developers' Workshop*. San Luis Obispo, CA, USA,.
- MAD-1101, Bigelow, A., Hawkins, C., Advisor: Demetriou, M. A. 2011. *Attitude Determination and Control, On Board Computing, and Communication Subsystem Design for a CubeSat Mission*. MQP, Worcester, MA: Worcester Polytechnic Institute.
- MAD-1201, Dawson, E., Nassiff, N., Velez, D., Advisor: Demetriou, M. A. 2012. *Determination and Control System Design for A CubeSat Mission*. MQP, Worcester, MA: Worcester Polytechnic Institute.
- MAD-1301, Farhat, A. T., Ivase, J. T., Lu, Y., Snapp, A. T. 2013. *Attitude Determination and Control System for CubeSat*. MQP, Worcester, MA: Worcester Polytechnic Institute.
- Markley, F. L., and Crassidis, J. L. 2015. *Fundamentals of Spacecraft Attitude Determination and Control*. New York: Space Technology Library, Springer.
- Moore, G., Holemans, W., Huang, A., Lee, J., McMullen, M. and et al. 2010. "3D Printing and MEMS Propulsion for the RAMPART 2U CUBESAT." *AIAA/USU Conference on Small Satellites*.
- Murray, W., and Ng, K. M. 2010. "An algorithm for nonlinear optimization problems with binary variables." *Computational Optimization and Applications* 47 (2): 257-288.
- NAG-1002, Oliva, A., Schaalman, G., Stalety, S., Advisor: Gatsonis, N. A. 2011. *Design and Analysis of Subsystems for a CubeSat Mission*. Worcester, MA: Worcester Polytechnic Institute.

- NAG-1102, Dopart, C., Morlath, R., Oliver, E., and Schomaker, J. 2012. *Design and Analysis for a CubeSat Mission*. MQP, Worcester, MA: Worcester Polytechnic Institute.
- NAG-1204, Billings, D., Graedel, I., Hoey, F., Lavallee, P., Martinez, N., and Torres, J., Advisor: Gatsonis, N. 2013. *Design and Analysis for a CubeSat Mission*. MQP, Worcester, MA: Worcester Polytechnic Institute.
- NAG-1302, Eslava, S., Marchetto, and J. Scougal, E. 2014. *Design of a μ -Pulsed Plasma Thruster for a 3U CubeSat*. MQP, Worcester, MA: Worcester Polytechnic Institute.
- Oppenheimer, M. W., and Doman, D. B. 2006. *Control Allocation for Over-Actuated Systems*. Air Force Research Lab.
- Roethlisberger, G., Jordan, F., Servonet, A., Borgeaud, M., Krpoun, R., and Shea, H. R. 2008. "Advanced Methods for Structural Machining and Solar Cell Bonding Allowing High System Integration and their Demonstration on a Pico-satellite." *22nd AIAA/USU Conference on Small Satellites*.
- Shaw, P. V. 2011. *Pulsed Plasma Thrusters for Small Satellites*. University of Surrey.
- Shaw, P. V., and Lappas, V. J. 2011. "Design, development and evaluation of an 8 μ PPT propulsion module for a 3U CubeSat application." *International Electric Propulsion Conference*. Wiesbaden, Germany.
- Sidi, M. J. 2000. *Spacecraft Dynamics and Control: A Practical Engineering Approach*. UK: Cambridge University Press.
- Sundaramoorthy, P. P., Gillm, E., Verhoeven, C. J. M., and Bouwmeester, J. 2010. "Two CubeSats with μ -Propulsion in the QB50 Satellite Network." *AIAA/USU Conference on Small Satellites*. Utah.
- Visser, F. 2014. "A Technical Background of the ZACUBE-i Satellite Mission Series." *11th Annual CubeSat Developers' Workshop - The Edge of Exploration*.
- Wahba, G. 1965. "A Least Squares Estimate of Spacecraft Attitude." *SIAM Review* 7 (3).
- Wertz, J. R. 1980. *Spacecraft Attitude Determination and Control*. Boston/London: Kluwer Academic Publishers.
- Wertz, J. R., and Larson, W. J. 2008. *Space Mission Analysis and Design 3rd ed*. New York: Space Technology Library.
- Wie, B. 2008. *Space Vehicle Dynamics and Control, 2nd ed*. Reston, VA: AIAA Education Series, AIAA.
- Winch, D. E., Ivers, D. J., Turner, J.P.R., and Stening, R. J. 2005. "Geomagnetism and Schmidt quasi-normalization." *Geophysical Journal International* 160 (2): 487-504.